LONG-WAVELENGTH INFRARED THERMOPHOTONIC IMAGING OF DEMINERALIZATION IN DENTAL HARD TISSUE

ASHKAN OJAGHI

A THESIS SUBMITTED TO THE FACULTY OF GRADUATE STUDIES
IN PARTIAL FULFILLMENT OF THE REQUIREMENTS FOR THE DEGREE OF
MASTER OF APPLIED SCIENCE

GRADUATE PROGRAMME IN MECHANICAL ENGINEERING
YORK UNIVERSITY
TORONTO, ONTARIO

AUGUST 2016

ABSTRACT

Early detection of the most prevalent oral disease worldwide, i.e., dental caries, still remains as one of the major challenges in Dentistry. Current dental standard of care relies on caries detection methods which lack the sufficient specificity and sensitivity to detect caries at early stages of formation when they can be healed. In this thesis, a clinically and commercially viable thermophotonic imaging (TPI) technology capable of detecting early enamel caries using an inexpensive long-wavelength infrared (LWIR, 8-14μm) camera is presented.

Through theoretical modelling and experiments on standard samples, the enhanced diagnostic contrast in LWIR detection compared to existing MWIR detection technologies is verified. Diagnostic performance of the system and its detection threshold are experimentally evaluated by monitoring the inception and progression of artificially-induced occlusal and proximal caries as well as natural early caries. The results are suggestive of the suitability of the developed LWIR system for detecting early dental caries.

To my mother and father.

TABLE OF CONTENTS

Table of Contents …….. iv

List of Tables ……...……. vi

List of Figures ……..……...……. vii

Chapter 1 Introduction ……...…… 1

1.1 Definition and history of photothermal phenomena …… 1

1.2 Fundamentals of Photothermal Radiometry ……...……. 6

1.3 Applications of photothermal radiometry and lock-in thermography …..…. 10

1.4 The objectives and outlook of the thesis ……...……. 16

Chapter 2 Early Dental Caries and Tooth Demineralization ……...…… 18

2.1 Prevalence and challenges in early detection and management …… 18

2.2 Human Tooth Structure ……. 19

2.3 Dental Plaque …… 21

2.4 Demineralization and Remineralization of Tooth ……..… 22

2.5 Light-matter interaction in turbid media ……... 23

2.5.1 Effects of Demineralization …… 27

2.6 Existing Optics-based early caries detection technologies …… 28

Chapter 3 Materials, Instrumentation, and Methods ……... 32

3.1 Experimental Setup ……... 32

3.2 Synchronous undersampling ……. 35

3.3 Samples ……. 37

3.3.1 Standard Opaque Sample ……... 37

3.3.2 Dental Samples …….. 37

3.3.3 Controlled Demineralization Protocol ……... 38

Chapter 4 Theoretical Modelling …… 41

4.1 Theory ……... 41

4.2 Theoretical modelling of caries detection in the MWIR and LWIR bands ... 45
Chapter 5 Thermophotonic Lock-in Imaging …….. 50
5.1 Basic principles of thermal-waves ……. 50
5.2 Validation of the developed LWIR TPLI system …….. 53
5.3 Detection of dental caries ……... 55
5.3.1 Detection of proximal caries ……...…… 56
5.3.2 Detection of occlusal caries …… 62
5.3.3 Detection of Natural Occlusal Caries ……. 65
5.3.4 Determination of Detection Threshold ……... 68
Chapter 6 Conclusion, Shortcomings, and Future Directions ……. 71
6.1 Conclusion ……. 72
6.2 Shortcomings and Future Directions ……. 70
References …… 75

LIST OF TABLES

Table 2.1 Absorption and scattering properties of sound and carious enamel, [45] with modification …… 26

Table 2.2 Thermal properties of sound enamel [45] …….…….. 28

LIST OF FIGURES

Figure 1.1 Excitation and propagation of thermal waves [1] ……..…… 2

Figure 1.2 A schematic representation of Bell's Photophone [2] …….. 3

Figure 1.3 Schematic representation of different detection schemes [4] ……... 4

Figure 1.4 Photothermal Radiometry setup for detection of the thermal-waves …...…… 6

Figure 1.5 (a) Experimental setup for pulsed thermography (b) Thermal image after optical excitation showing shallow (A), intermediate (B), and deep (C) defects as well as a semi-infinite point (R) PT cooling profiles (c) before and (d) after baseline reduction [6] ……...….. 8

Figure 1.6 (a) Photothermal radiometry setup in transmission mode. (b) Variation of photothermal amplitude and phase with sample thickness at several modulation frequencies [9] ……. 11

Figure 1.7 Photothermal subsurface structure detection. Unlike the amplitude channel, photothermal phase has enough sensitivity to detect the 1mm-diameter holes [9] …..... 12

Figure 1.8 Remote probing of coating thickness and defects. Arrows indicate the presence of subsurface defects [11] ……...……. 13

Figure 1.9 Experimental setup for lock-in thermography [12] …… 14

Figure 2.1 Section of human molar [6] …...……. 20

Figure 2.2 Light-tissue interaction mechanisms …….. 24

Figure 2.3 (a) Attenuation coefficient of enamel and water at near infrared wavelengths [43]. (b) Enamel infrared transmission spectrum [44] ……. 26

Figure 3.1 (a) The experimental setup consisting of a NIR laser, an LWIR camera, a frame grabber, and a multifunctional DAQ device. (b) Signal processing algorithm 33

Figure 3.2 Synchronous undersampling of a high frequency wave form using a low sampling rate. One modulation cycle is sampled out of each 12 consecutive cycles [53] …….…….. 36

Figure 3.3 Opaque standard sample with three holes …….……. 37

Figure 3.4 Submerged dental sample in the acidic gel …….…….... 39

Figure 4.1 Phase and amplitude of the theoretical radiometric signal calculated for MWIR and LWIR detection spectral bands from absorbers located at different depths.

Normalized amplitude values for (a) LWIR ($\bar{\mu}_{IR}$ =50000 m^{-1}) and (b) MWIR ($\bar{\mu}_{IR}$ =100 m^{-1}). Normalized phase values for (c) LWIR ($\bar{\mu}_{IR}$ =50000 m^{-1}) and (d) MWIR ($\bar{\mu}_{IR}$ =100 m^{-1}) ……..……. 47

Figure 4.2 Theoretical radiometric signal phase vs. absorber depth for several μ_{IR} values ……..……. 48

Figure 4.3 Theoretical radiometric signal amplitude vs. absorber depth for several μ_{IR} values ……...…… 49

Figure 5.1 Normalized phase images of blind holes with different depths obtained at (a) 5 Hz, (b) 10 Hz, and (c) 20 Hz, respectively ……..…… 55

Figure 5.2 Optical image of the sample with proximal caries (a) before and (b) after 10 days of demineralization on the treatment window. Normalized TPLI amplitude images of sample (c) before and after (d) 2, (e) 4, (f) 6, (g) 8, and (h) 10 days of treatment ….. 57

Figure 5.3 (a) Amplitude profiles along the dashed line shown in Figure 5.2(h) and (b) the average normalized amplitude values within the treatment window ……. 58

Figure 5.4 TPLI Phase images of sample with proximal caries(a) before and after (b) 2, (c) 4, (d) 6, (e) 8, and (f) 10 days of treatment …… 59

Figure 5.5 (a) Phase profiles along the dashed line shown in Figure 5.4(f) and (b) average phase values within the treatment window for samples at several demineralization stages …….. 62

Figure 5.6 Optical image of the sample (a) before and (b) after 10 days of demineralization on the treatment window. TPLI phase images of sample (c) before and after (d) 2, (e) 4, (f) 6, (g) 8, and (h) 10 days of treatment obtained at 2 Hz modulation frequency ……. 64

Figure 5.7 Average phase values within the treatment window for samples at several demineralization stages ……..……. 65

Figure 5.8 Optical image (a) of the occlusal surface of tooth sample. Thermophotonic amplitude (b) and phase (e) images of the occlusal surface obtained at 1 Hz. Thermophotonic amplitude (c) and phase (f) images of the occlusal surface obtained at 5 Hz. Thermophotonic amplitude (d) and phase (g) images of the occlusal surface obtained at 20 Hz ……..……. 67

Figure 5.9 Average phase values within the treatment window for the sample at several demineralization stages. The dashed line indicates the detection threshold of our low-cost LWIR TPI system …… 70

Figure 6.1 Designed clinically viable imaging platform ……. 74

Chapter 1

Introduction

This chapter introduces the photothermal effect and provides a short history on the development of photothermal radiometry and lock-in thermography. Applications of these methods along with the motivation for their use in medical diagnosis are also discussed.

1.1 Definition and history of photothermal phenomena

Photothermal science is a broad field, encompassing a wide spectrum of instrumentation techniques which work based on the photothermal effect. In these techniques, an intensity modulated oscillating excitation source is used to induce heat in a material through a series of optical absorption events. As a result, an oscillating temperature field is generated inside the sample which propagates into the medium (Figure 1.1). This modulated temperature field which is also known as the thermal-wave field, carries information about the sample and can be detected in a variety of different ways. For instance, in photothermal radiometry, the infrared radiation emanating from the thermal-wave field at object's surface is acquired using an infrared detector in a non-contact manner. Or, alternatively in the photoacoustic method, the sample response is probed via detection of the sound waves that are generated at the absorption site as a result of thermoelastic volume expansion which transmit to the detector through a coupling medium on sample surface.

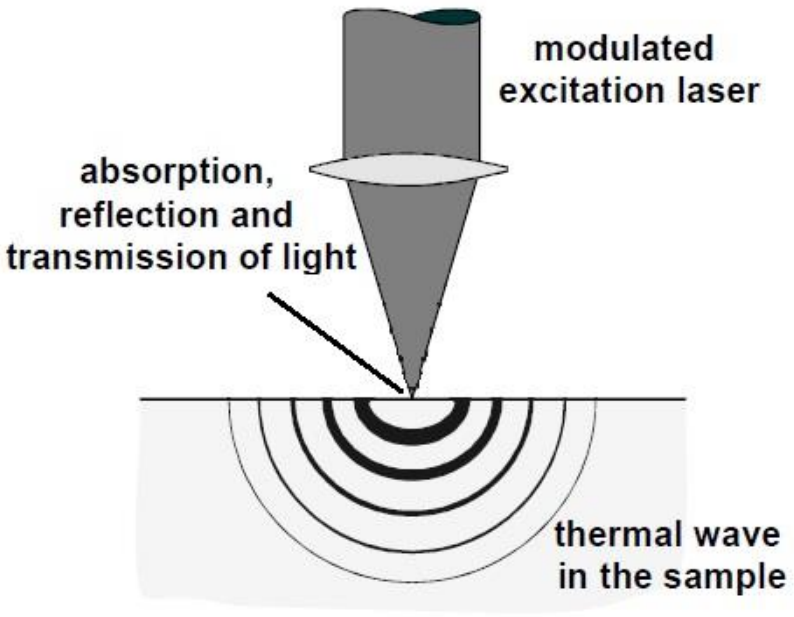

Figure 1.1 Excitation and propagation of thermal waves [1]

One of the first devices designed based on the photothermal effect was the photophone invented by Alexander Graham Bell in 1880 [2]. Bell's photophone (Figure 1.2) worked based on transmission of photoacoustic waves generated as a result of modulation of the sunlight rays reflected by a mirror that was vibrating with human voice. The detection was photoacoustically carried out at the receiver's end through absorption of light by crystalline selenium cells followed by thermoelastic volume expansion and sound waves generation. However, Bell did not expand his idea of photophone as he encountered many difficulties transmitting the modulated sun light through open air.

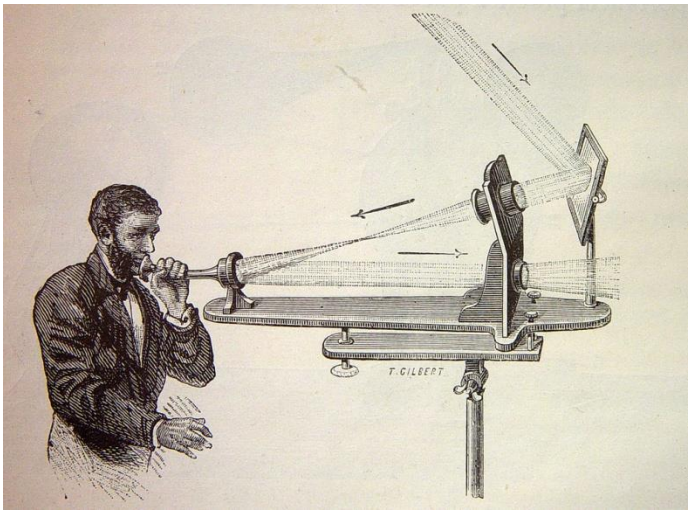

Figure 1.2 A schematic representation of Bell's Photophone [2]

Almost a century later, in 1976 Allan Rosencwaig and Allen Gersho developed a correct theoretical foundation for the photoacoustic effect [3], leading to the rapid development of the field and invention of several other detection schemes (schematically shown in Figure 1.3).

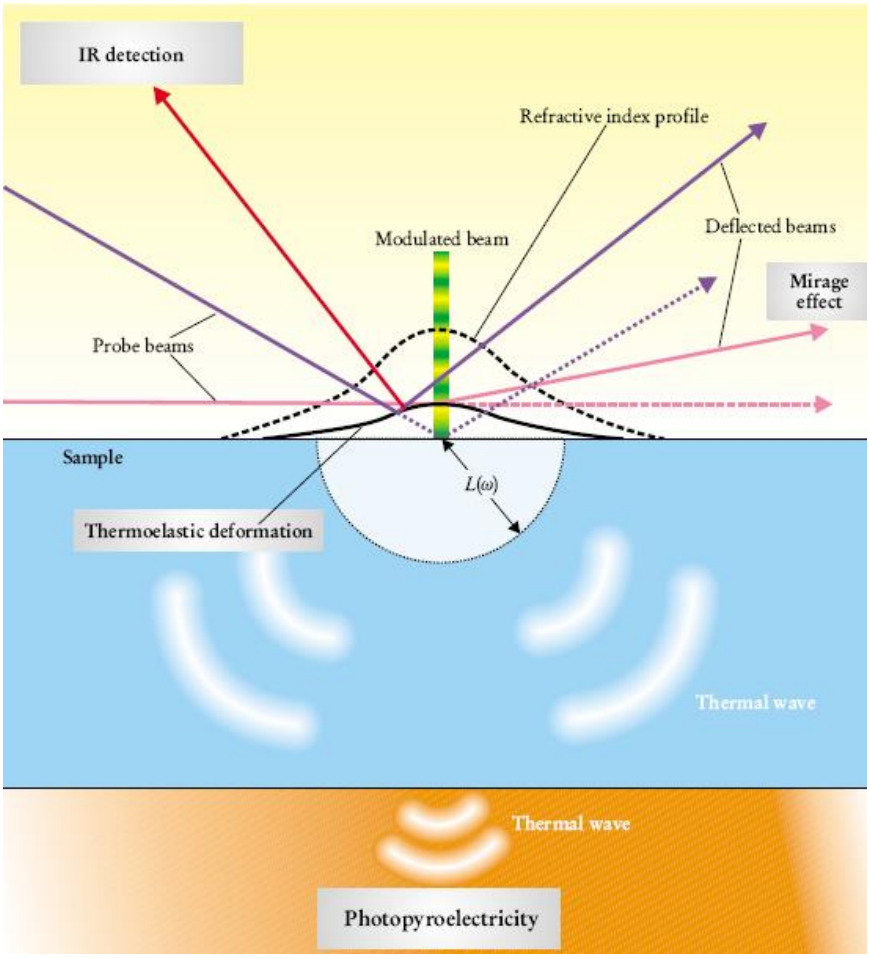

Figure 1.3 Schematic representation of different detection schemes [4].

Among the proposed detection methods, photothermal radiometry (PTR) [5] first developed by Nordal and Kanstad in 1979 (Figure 1.4 [1]) has gained substantial attention as the one of the methods that directly measures the temperature of the sample in a non-contact manner through an infrared detector and based on the Stefan-Boltzmann law:

$$W = \varepsilon\sigma T^4 \tag{1.1}$$

here W is the total radiant emittance from the interrogated point, σ is the Stefan-Boltzmann constant (5.67×10^{-12} W cm^{-2} K^{-4}), and ε is the emissivity.

A conventional photothermal radiometric setup is shown in Figure 1.4. Here, the thermal-wave field is generated inside the sample by absorption of the intensity-modulated light (either pulse or continuous wave) that is delivered via a laser diode. Radiometric detection is done using a cooled IR-detection device (e.g., a liquid nitrogen cooled MCT = mercury cadmium telluride-detector) which monitors the thermal response and the variations of the surface temperature. For a small change in sample temperature, δT, the change in radiant emittance will be linear and can be found as:

$$\delta W = 4\varepsilon\sigma T^3 \delta T \tag{1.2}$$

As such, PTR systems can reliably register the temperature change contributions of subsurface sources (e.g., absorbers, defects) through radiometric interrogation of sample surface.

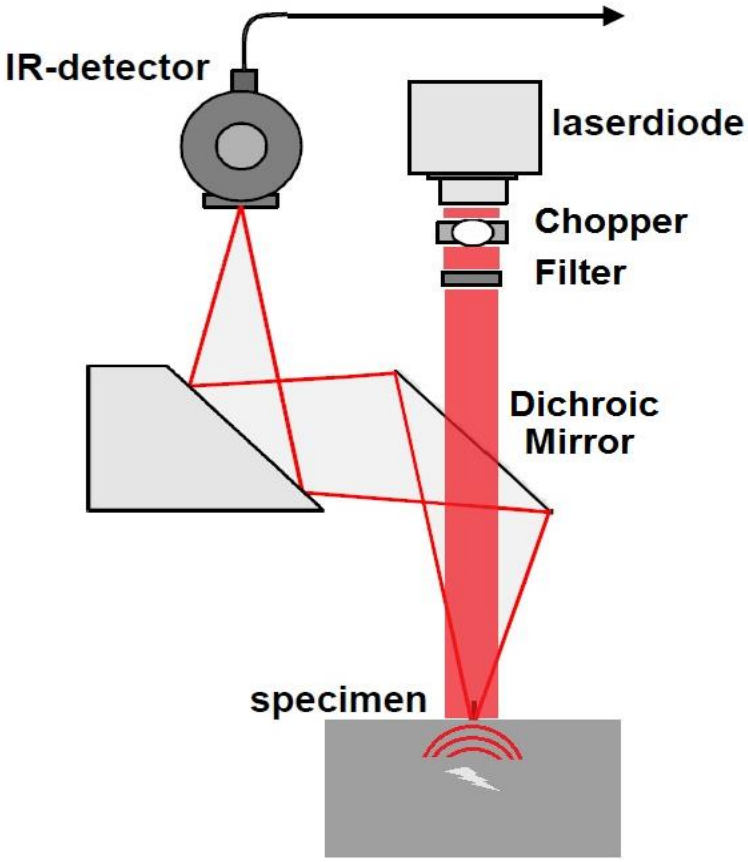

Figure 1.4 Photothermal Radiometry setup for detection of thermal-waves

1.2 Fundamentals of Photothermal Radiometry

Photothermal radiometry can be classified based on different criteria such as the type, wavelength, and intensity of optical excitation. In general, two kinds of optical excitation schemes can be used in PTR: pulse or continuous-wave excitation.

In pulse PTR, a short (few milliseconds or a few seconds for low thermal conductivity materials) high-power optical pulse is applied to the sample and its subsequent thermal evolution is recorded either with a single infrared detector (pulse photothermal radiometry, P-PTR) or with an infrared camera (pulse thermography, PT). The temporal temperature

evolution in this method involves a rise at first due to the applied pulse excitation then it decays as heat is dissipated to the bulk of the specimen as a result of heat diffusion process [6]. However, the heat dissipation rate is reduced over subsurface defects and as a result the defective area appears as an area of higher temperature compared to the surrounding medium which will lead to a change in the cooling profiles over the defects, Figure 1.5. Due to reduced heat dissipation rate the cooling rate over the defective regions will be decreased as evident in cooling profiles of Figure 1.5(d). This will also lead to an enhanced infrared emission from the sample and subsequent registration of a stronger radiometry signal by the detector which will eventually lead to appearance of defects in the thermal image shown in Figure 1.5(b).

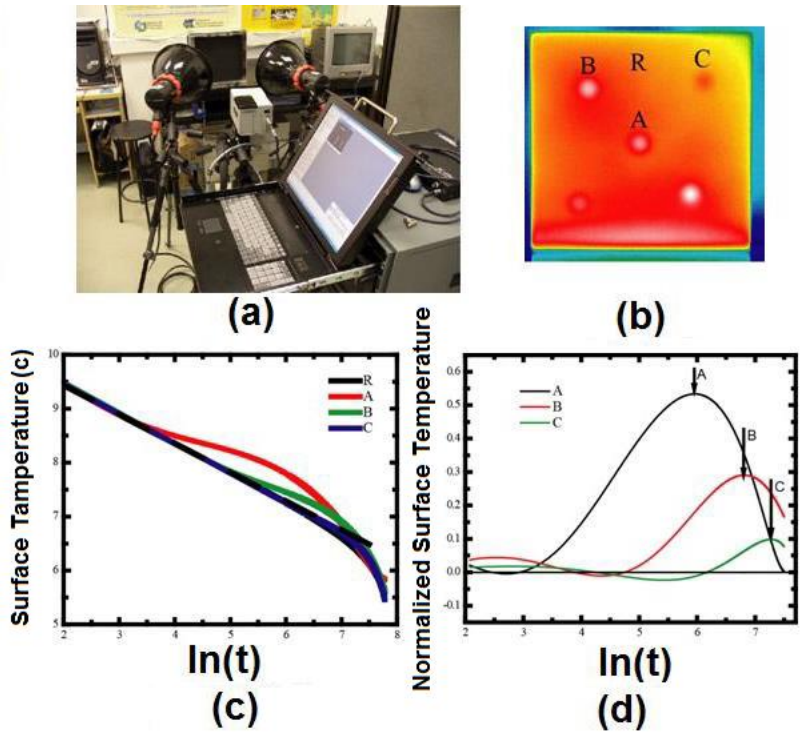

Figure 1.5 (a) Experimental setup for pulsed thermography (b) Thermal image after optical excitation showing shallow (A), intermediate (B), and deep (C) defects as well as a semi-infinite point (R) PT cooling profiles (c) before and (d) after baseline reduction [6]

Several signal processing methods have been proposed to improve the performance of PT. The most common one is where the temperature decay profile of a semi-infinite area is subtracted from those of defective areas to magnify the time-delayed energy accumulation caused by the subsurface defects, Figure 1.5(d). In pulse method, thermal waves are generated in a wide range of frequencies and the sample response is investigated in time-domain and in a transient mode, making it an arduous task to study the contribution of individual frequency components. Moreover, the results are of amplitude nature and therefore very prone to non-uniformities in applied excitation, sample emissivity,

reflections from ambient, and sample surface conditions. However, pulse method seems to be the most popular method in industrial non-destructive testing applications mainly due to its speed and ease of interpretation.

Fourier (1822) [7] was the first who laid the theoretical foundation of frequency-domain photothermal radiometry in which he showed that heat conduction problems in solids can be solved by expanding the applied excitation as a series of waves at different frequencies. Afterwards, Ångström (1863) [8] expanded this theoretical explanation by proposing a "temperature-wave" method for the determination of thermal diffusivity in a long rod. As a result, this methodology is also referred to as Fourier-domain photothermal radiometry or FD-PTR. In this method, the excitation is in the form of low-power, continuous, amplitude-modulated pattern at a given temporal frequency and the outcome is a spatially-damped thermal-wave field inside the sample at the applied excitation frequency. The signal processing of FD-PTR is not as straight forward as its pulse counterpart and requires quadrature demodulation of the signal to retrieve the amplitude and phase information of the thermal waves. FD-PTR has unique advantages over P-PTR; the most important advantage is that it can provide an additional contrast parameter (phase channel) which is emissivity normalized [9, 10] and therefore insensitive to variations in the applied excitation power and/or sample surface conditions. Lock-in thermography is the 2D extension of FD-PTR where the single IR detector is replaced by an array of IR detectors (i.e., infrared camera).

1.3 Applications of photothermal radiometry and lock-in thermography

Since the introduction of photothermal radiometry as a non-contact and non-invasive diagnostic technique for inspection of materials, a wide range of applications have been proposed for the method. The majority of the applications are intended for non-destructive evaluation and testing (NDE & T) of industrial materials. Gerhard Busse [9] was one of the first who used photothermal radiometry for NDT. Figure 1.6(a) shows one of his early studies in 1980 for measuring the thickness of an Aluminum wedge sample through measurement of the amplitude and phase of the transmitted thermal waves. The experimental setup included an Ar-ion laser emitting at 488 nm. The laser beam was modulated between 15Hz to 30Hz and was then focused on the sample while the transmitted thermal waves were monitored by the infrared detector (Golay cell) from the back of the sample. The amplitude line scans of Figure 1.6(b) show that the transmitted thermal wave amplitude decreases exponentially as the sample thickness increases. This trend highlights the spatially damped nature of thermal waves. Moreover, the larger the sample thickness, the larger is the phase shift due to the longer path travelled by the thermal waves.

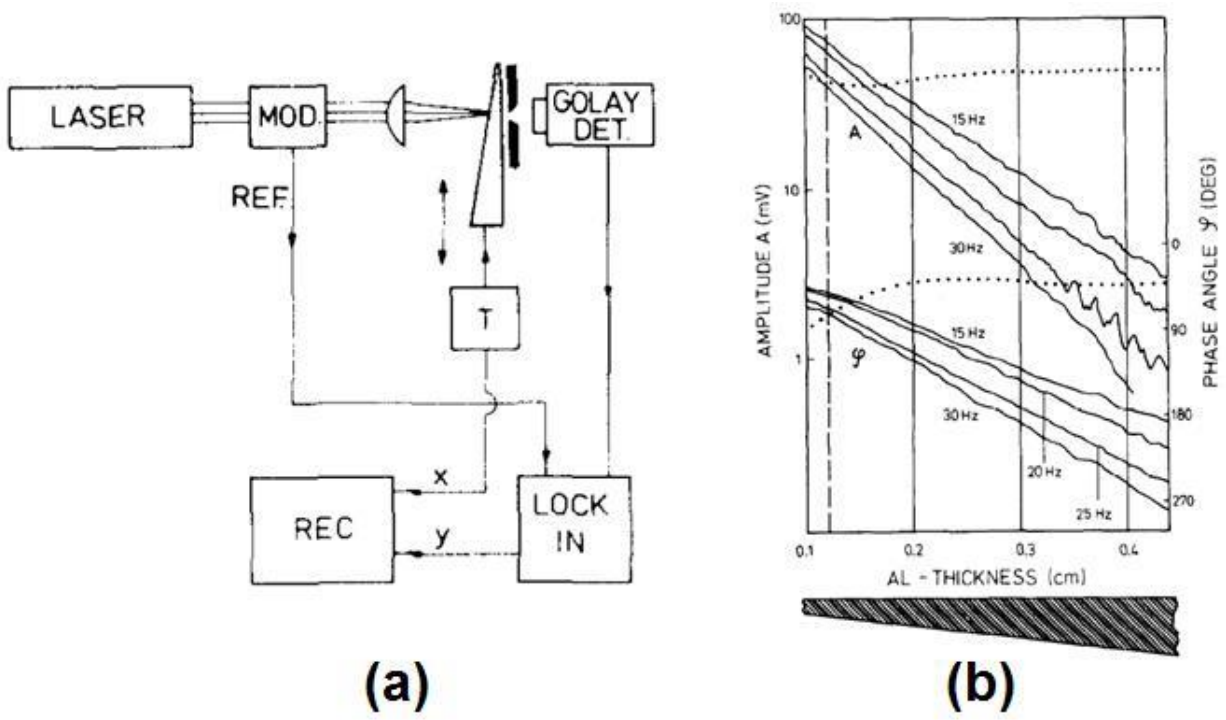

Figure 1.6 (a) Photothermal radiometry setup in transmission mode. (b) Variation of photothermal amplitude and phase with sample thickness at several modulation frequencies [9]

Using the same experimental setup, this study showed that photothermal phase can detect subsurface holes parallel to the interrogated surface, while the photothermal amplitude lacks the sufficient sensitivity to detect such subsurface features (Figure 1.7). The improvement in sensitivity is due to the emissivity normalized nature of the phase channel.

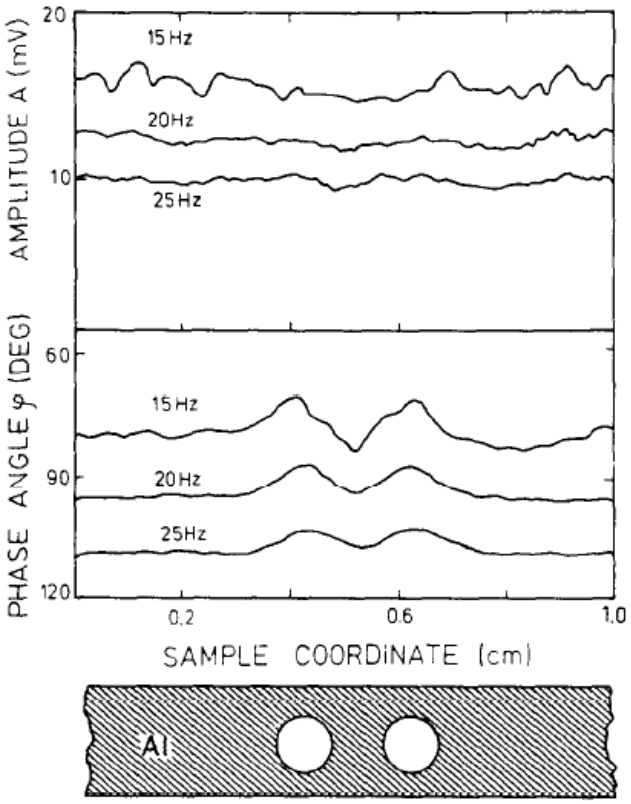

Figure 1.7 Photothermal subsurface structure detection. Unlike the amplitude channel, photothermal phase has enough sensitivity to detect the 1mm-diameter holes [9]

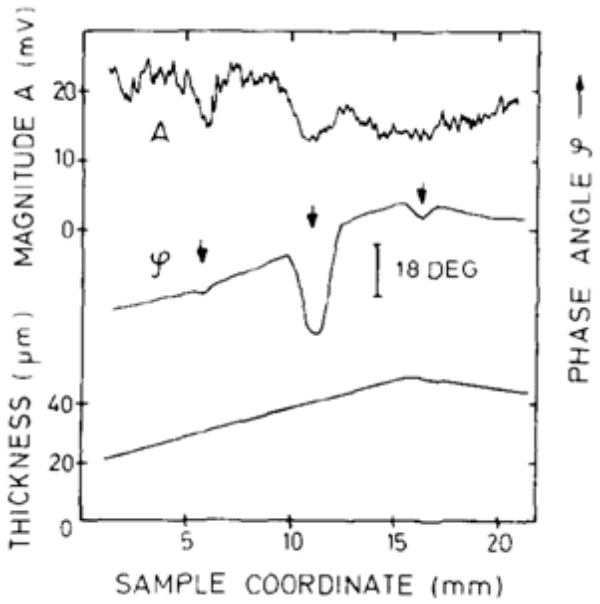

Figure 1.8 Remote probing of coating thickness and defects. Arrows indicate the presence of subsurface defects [11]

Busse expanded the NDT applications of FD-PTR to detection of polymer coating defects on an aluminum substrate using a similar experimental setup in 1983 [11]. He demonstrated that phase channel is more sensitive to subsurface variations in thermophysical properties than the amplitude channel (Figure 1.8). He also was able to determine the coating delamination by adding a thin layer of grease underneath the polymer coating and detecting it using the FD-PTR phase measurements.

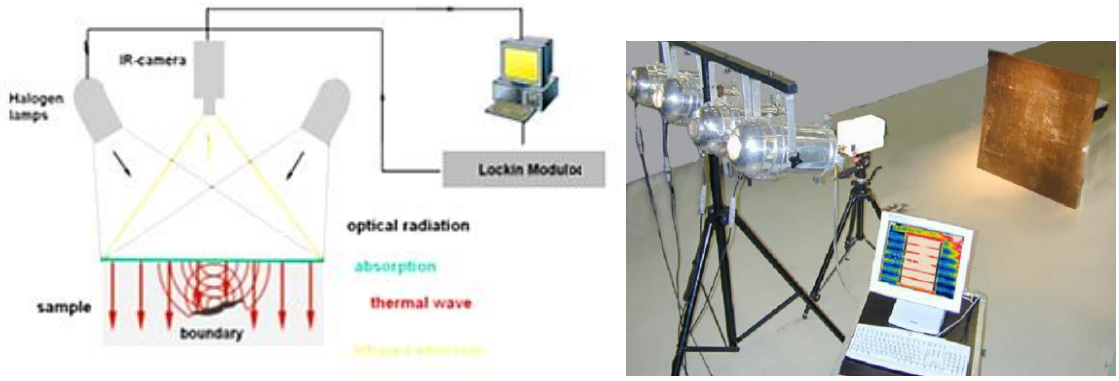

Figure 1.9 Experimental setup for lock-in thermography [12]

Although in the early days of PTR promising results were achieved using FD-PTR for NDE applications, the extremely long measurement time required to inspect the whole sample through a surface raster scan limited the adaptation of this method in industry. This problem was solved in late 1970's to early 1990's by the introduction of infrared camera to the FD-PTR setup [13-16]. The new system was called lock-in thermography (LIT) (Figure 1.9) which increased the inspection speed of the PTR system by imaging a large area on the surface of the object by focusing the infrared camera on the sample.

The earliest applications of lock-in thermography can be found in the studies conducted by researchers such as Karpen *et al.* [17] who used this method to acquire information about the fiber orientation in composites. Wu e*t al.* [18] also studied the delamination of veneered wood and used thermography to visualize the delaminations. In another study Wu e*t al.* [19] applied lock-in thermography on thickness, density, and porosity measurement of ceramic coatings. In a more comprehensive study Meola *et al.* [20] investigated the capability of this method in measurements of material thermal diffusivity, visualization of different kinds of damage in different materials, evaluation of the HAZ extension in AISI

welded joints, as well as control of bonding improvements after surface plasma treatment. This method also found its way to other applications such as inspection of aircraft structural components [21] and evaluation of shunt defects in solar cells [22].

Other researchers expanded the use of lock-in thermography further to applications such as detection of voids and cracks in glass fiber reinforced composites and polymers [20, 23]. Giorleo *et al.* [24] studied the defects in carbon-epoxy laminates by means of a lock-in thermography system and a long-wave infrared camera. In a more recent study An *et al.* [25] investigated the use of laser lock-in thermography for detection of surface-breaking fatigue cracks on uncoated steel structures. The technique used in this study could successfully resolve the surface-breaking cracks on the samples.

Looking at the PTR/LIT literature, it can be realized that despite the widespread implementation of these techniques in non-destructive evaluation of industrial materials [20, 23-25], a limited number of studies have looked into the use of active thermography for diagnostic imaging of biomedical samples.

Among the first studies incorporating lock-in thermography for medical diagnosis were the ones conducted by John and Salerno [26] and John et al. [27]. They examined the ground section of a resin-embedded extracted human tooth using modulated optical excitation and lock-in thermography. However, the result of their study was limited only to estimation of the relative thermal thicknesses of dental samples and no diagnostic study was carried out. In a more recent study, Tabatabaei et al. [28, 29] used thermophotonic lock-in imaging (TPLI) to detect early stages of demineralization in dental tissues using a research-grade mid-wavelength infrared (MWIR) camera. The study demonstrated the great potential of

TPLI for detecting early dental caries and its diagnostic outperformance over other emerging technologies [30]; however, the IR camera used in this study was an expensive (~USD $80k) research-grade camera with integrated cryogenic cooling system not suitable for commercialization and clinical translation to Dentistry. As such, this thesis takes the first step in translation of TPLI technology into Dentistry by studying the diagnostic performance of an economically viable LWIR thermophotonic lock-in imaging system for detecting early dental caries.

Recent advances in the field of microelectronics have enabled the design and manufacturing of long-wave infrared (LWIR) and uncooled microbolometer detector arrays which no longer require integrated cryogenic cooling systems, leading to a reduction in the size, weight, and cost of the IR cameras. In addition to affordability and small form factor, the use of LWIR over MWIR detectors for interrogation of samples at near ambient temperatures is advantageous as the peak of the black body radiation falls in the LWIR band (~ 9μm) at room temperature, providing considerably higher photon flux to the detector.

1.4 The objectives and outlook of the thesis

As mentioned earlier, the existing thermophotonic imaging technologies which work in the MWIR detection spectral band are not suitable for integration into a commercially and clinically viable dental diagnostic device due to their high overall cost and weight. To effectively address this issue, this thesis focuses on the development of a low-cost thermophotonic lock-in imaging system for detection of early dental caries using an

inexpensive LWIR infrared camera. This study, to date, is the first report on the application of active thermography in the LWIR band for diagnostic imaging of biological samples (i.e., detection of early dental caries).

Since thermophotonic lock-in imaging is performed on dental samples, chapter 2 of this thesis is dedicated to the dental background required for proper understanding of experiments carried out on these samples.

Chapter 3 describes the instrumentation and signal processing methodologies used in the thesis. Moreover, in this chapter the procedure for sample and acidic gel preparation are described.

Chapter 4 presents the theoretical background and the discussion on the detection sensitivity improvement of the system through modelling of detection in LWIR and MWIR spectral regions.

Thermophotonic lock-in imaging of standard opaque samples and early dental caries are discussed in chapter 5. This chapter presents the thermal-wave theory as well as the thermophotonic imaging of opaque standard sample done as a proof of concept. Furthermore, the capabilities of the developed system in early caries detection are discussed through experiments on artificially-induced and natural proximal and occlusal caries. Lastly, the detection threshold of the system at very early demineralization is investigated experimentally.

Chapter 6 brings together the conclusions of the research presented in this thesis.

Chapter 2

Early Dental Caries and Tooth Demineralization

In this chapter ample background on the characteristics of human tooth as well as the demineralization and early caries formation mechanisms is provided for the reader to follow the discussions made in the following chapters on the diagnostic imaging of early dental caries. The chapter opens with a brief explanation on the prevalence of early dental caries and the challenges in their diagnosis and management. Then the structure of human tooth along with the demineralization and caries formation mechanisms in dental tissues are discussed. In the final section, the light-matter interaction in dental hard tissue as a turbid medium is explained.

2.1 Prevalence and challenges in early detection and management

Dental caries is an oral infection identified as the most prevalent dental disease among children and adult populations worldwide and is the lead cause of tooth loss [31, 32]. The inception of tooth decay in caries starts with minute amounts of mineral loss (i.e., demineralization) from the enamel surface as a result of the decomposition of hydroxyapatite crystals in the acidic environment of dental plaques [33]. If a prolonged acidic environment is maintained, early caries progress deep into the enamel and form a cavity which necessitates costly and labor-intensive surgical interventions. However, if dental caries are detected early enough, their progression can be stopped (i.e, arrested caries) or even reversed (i.e. healed/remineralized) though preventive actions such as oral hygiene counseling or fluoride therapy [34]. According to a study conducted by Abanto et

al. [35], tooth decay has been more common than asthma among 5-17 year olds and is responsible for many missed days from school and work. Reports published by the U.S. Department of Health and Human Services [36] and the U.S. National Institute of Dental and Craniofacial Research [[37] also suggest that, by age 19, 68% of youth have experienced tooth decay, and 92% of adults aged between 20 to 64 have had dental caries in their permanent teeth. To effectively address this prevalence, dentistry is undergoing a paradigm shift away from interventional treatment of caries to a medical model of disease prevention and management, involving early detection of caries. Conventionally, dental standard of care relies on surgical treatment where caries detection is conducted through visual/tactile inspection and X-ray radiography. These detection methods, however, lack the sufficient sensitivity and specificity to detect caries in early stages of formation. Therefore, use of X-ray radiography in clinical Dentistry is currently limited to detection of well-developed cavities [38]. As such, the National Institutes of Health consensus statement published in 2003 has identified the development of reliable methods for detecting early dental caries as one of the major areas in which more research is needed [39].

2.2 Human Tooth Structure

Enamel, dentin, pulp, and cementum are the four types of tissue that make up human tooth. Enamel, as the hardest and most mineralized tissue in the body, consists of mineral (ninety-five percent), as well as water and organic materials. Sound enamel is made up of tightly packed hydroxyapatite crystals ($Ca_5(PO_4)_3OH$), giving the enamel a glass-like appearance, also making it a translucent (refractive index of 1.62) material with yellow-white color

[40]. The enamel crystals are packed in a repeating arrangement, forming the enamel prisms. Even though crystal packing is very tight at the microscopic level, each crystal is separated from its neighbors by tiny inter-crystalline spaces filled with water and organic materials. The inter-crystalline spaces together form a network of diffusion pathways which are known as micro-pores in the enamel. The enamel microstructure is highly inhomogeneous, as a result of constant interaction of enamel crystals with oral environment through micro-pores. Enamel varies in thickness over the surface of the tooth and is as thick as 2.5 mm at the cusp, and thinnest at the cementoenamel junction (CEJ) as shown in Figure 2.1.

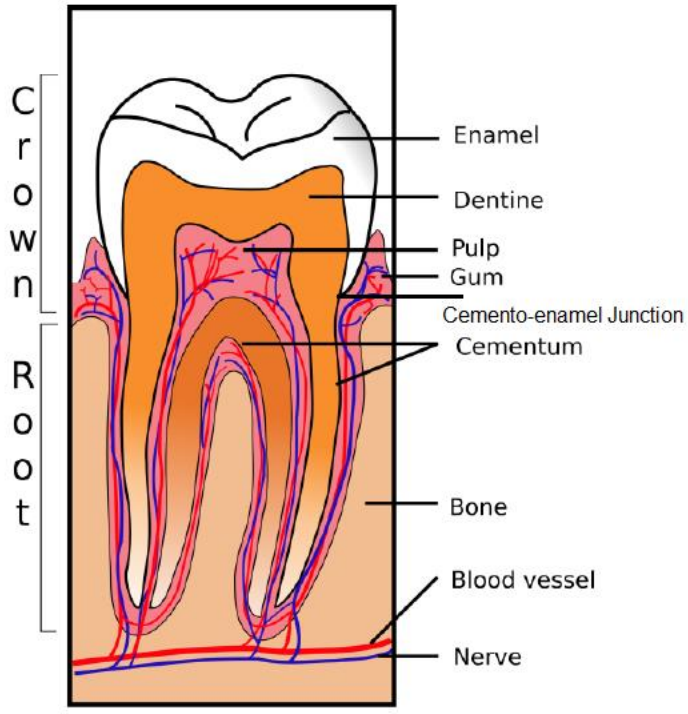

Figure 2.1 Section of human molar [6]

Dentin is the hard tissue between enamel and the pulp which is generally less mineralized than enamel and therefore softer than enamel. Dentin has microscopic channels, called dentinal tubules, which are radially placed through the dentin from the pulp cavity to the exterior cementum or enamel border. The dental pulp is the central part of the tooth filled with soft tissue. This tissue contains blood vessels and nerves that enter the tooth from a hole at the top of the root. The other tissue in the tooth is the Cementum which is a specialized bony substance covering the root of a tooth. Its coloration is yellowish and it is softer than either dentin or enamel [40].

2.3 Dental Plaque

Dental plaque is an adherent deposit of bacteria that grows on surfaces of the mouth. Glycoprotein from saliva forms a biofilm on the surface of enamel called “pellicle” which can attract specific types of bacteria to the tooth surface. The bacteria in the dental plaque are able to decrease the pH of the oral environment to below 5 by consuming fermentable carbohydrates (i.e. sugars sucrose and glucose). They are also able to synthesize a gelatinous sticky polymer of glucose that thickens the plaque layer and prevents saliva from neutralizing the plaque pH. Bacterial plaque is an essential precursor of caries and therefore regions with high concentration of bacteria (lower pH level) on the tooth surface are potentially prone to caries formation. It is worth mentioning that the caries formation mechanism is an alternating process of destruction and repair. When the destructive forces outweigh the reparative ability of the saliva (occurs at low pH) the process will progress (demineralization) and conversely if the reparative forces outweigh the destructive forces,

the process will stop or even reverse (remineralization) in the early stages of caries formation [40].

2.4 Demineralization and Remineralization of Tooth

As mentioned in the previous section, the micro-pores in the enamel are filled with water and as a result of their constant interaction with hydroxyapatite crystals of enamel, the water in the micro-pores is saturated with respect to hydroxyapatite, i.e. the mineral is in equilibrium with the ions in the solution [41]:

$$Ca_5(PO_4)_3OH \leftrightarrow 5Ca^{2+} + 3PO_4^{3-} + OH^- \qquad KSP_{HA}=7.41\times10^{-60} \quad [mol/l] \qquad (2.1)$$

where KSP_{HA} denote the solubility product of hydroxyapatite at 37°C. The solubility of hydroxyapatite and other calcium phosphates is greatly affected by the pH of the water in which it is dissolving. As indicated by 2.1, when PO_4^{3-} and OH^- accumulate in solution, together with calcium ions, dissolution of hydroxyapatite slows and stops as the solution becomes saturated. If acid is added, PO_4^{3-} ions and OH^- ions combine with H^+ to form HPO_4^{2-} ions and H_2O, respectively, thereby removing a proportion of PO_4^{3-} and OH^- ions from solution:

$$\begin{array}{l} Ca_5(PO_4)_3OH \leftrightarrow 5Ca^{2+} + 3PO_4^{3-} + OH^- \\ \qquad\qquad\qquad\quad \downarrow H^+ \quad \downarrow H^+ \\ \qquad\qquad\qquad\quad HPO_4^{2-} \quad H_2O \\ \qquad\qquad\qquad\quad \downarrow H^+ \\ \qquad\qquad\qquad\quad H_2PO_4^- \end{array} \qquad (2.2)$$

In this case the ion activity product of hydroxyapatite (IAP_{HA}) decreases, the solution is then said to be unsaturated ($IAP_{HA} < KSP_{HA}$) and more hydroxyapatite dissolves until saturation is re-established. As a result, mineral is removed from the hydroxyapatite crystals to compensate for the lack of ions in the solution and the inter-crystalline spaces enlarge and the tissue becomes more porous.

For remineralization to occur, the solution must be supersaturated with respect to hydroxyapatite ($IAP_{HA} > KSP_{HA}$). Thus, it is necessary to add the constituent ions to the solution either by adding calcium and/or phosphate separately or by raising the pH (increasing PO_4^{3-} and OH^- concentrations).

2.5 Light-matter interaction in turbid media

Light-matter interaction mechanisms in dental hard tissue as a turbid medium can be classified into four categories of transmission, scattering, reflection, and absorption which are schematically shown in Figure 2.2. Light scattering refers to path change of photons without any change in their energy; however, in an absorption event the photon energy is either completely converted to heat or partially converted to heat along with the emission of photons of lower energy (i.e. longer wavelength). These optical properties can be characterized by photon scattering (μ_s) and absorption coefficients (μ_a), which refer to the average number of absorption and scattering events per unit length of a photon propagating though the medium [42]. Using these parameters for a medium the total attenuation coefficient, which is an important optical parameter defining the total optical penetration depth, can be calculated as:

$$\mu_t = \mu_a + \mu_s \tag{2.3}$$

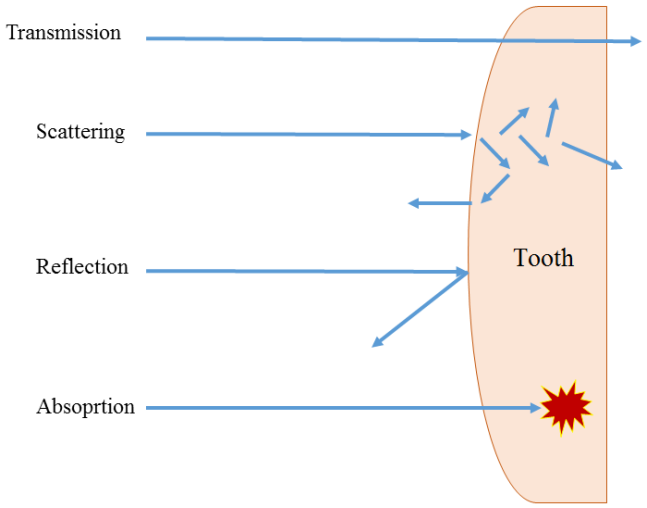

Figure 2.2 Light-tissue interaction mechanisms

As mentioned earlier, tooth is a multilayered and inhomogeneous structure, where each layer has its own thermal and optical properties. As a result, light propagation in teeth, similar to other biological tissues, is highly random and scattered, making the dental tissue a turbid medium. However, scattering of light in dental tissues is a function of the photons energy. That is, longer wavelengths (lower energy photons) are less scattered compared to the shorter wavelengths (higher energy photons) and can therefore penetrate deeper in the tooth structure. Light scattering by tooth in the near infrared wavelengths is highly forward directed, with mean cosine of scattering angle close to unity ($g \sim 1$) [6]. As a result, photons in near infrared wavelengths can penetrate deep into enamel and even dentine.

Although the amount of light scattering is a key factor in determining the light penetration depth, the photothermal signal is only generated as a result of light absorption. Therefore,

in order to ensure the proper generation of thermal wave, the wavelength of excitation beam should be carefully selected based on the scattering and the absorption coefficients of the dental tissue. Based on the attenuation spectra of water and enamel, the near infrared wavelengths (700 nm to 1200 nm) appears to be an ideal excitation range as laser light is not absorbed by water but slightly absorbed by enamel to generate thermal waves (Figure 2.3(a)). As such, the laser used in this study is working in the near infrared spectral region (808 nm).

The other important factor in thermophotonic imaging of dental tissues is the detection spectral region. Detection of infrared emission from absorbing regions within the tissue should be selected in a way that minimum amount of direct Planck radiation is reached to the detector from intact regions surrounding caries/defects. According to Figure 2.3(b) which shows the infrared transmission spectra of enamel, the transmission window in the 8-14 μm range (long-wavelength infrared) seems to be the optimal choice as the direct infrared (Planck) radiation from subsurface layers in tooth will be absorbed by the tissue, allowing for detection of conductive thermal waves, carrying subsurface information, by the infrared camera. A detailed discussion on the advantages of LWIR detection is provided in Chapter 4.

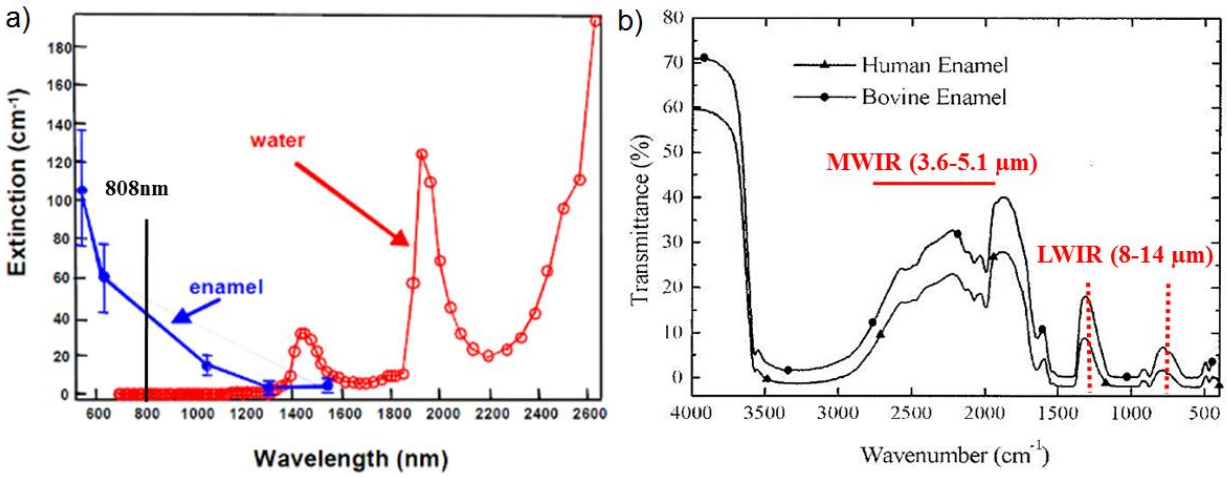

Figure 2.3 (a) Attenuation coefficient of enamel and water at near infrared wavelengths [43]. (b) Enamel infrared transmission spectrum [44].

Table 2.1 Absorption and scattering properties of sound and carious enamel, [45] with modification.

Wavelength (nm)	Absorption coefficient μ_a (m^{-1})	Scattering coefficient μ_s (m^{-1})
Sound Enamel		
543	< 100	10,500
600	< 100	3,300 - 7000
633	40 – 97	110 – 6600
700	< 100	2,700 – 5,500

800	< 100	3,300
1000	< 100	1,600
1053	< 100	1,500
Carious Enamel		
600	--	55,000
633	--	32,000 – 157,000

2.5.1 Effects of Demineralization

The absorption and scattering properties of sound and carious enamel are presented in Table 2.1. The tabulated optical properties of the carious and sound enamel suggest that absorption and scattering coefficients of carious enamel are significantly higher than those of intact enamel. Such increase occurs as a result of substitution of hydroxyapatite crystals with micro-pores during the demineralization process in the acidic environment of dental plaques. Presence of micro-pores in carious regions leads to enhanced local optical fluence due to high amount of scattering as well as optical absorption, leading to localization of heat generation within early caries which is the source of diagnostic contrast in the thermophotonic images. The infrared radiation from this enhanced temperature field can be detected by the infrared camera. The other interesting point is the large variation of data reported by different sources. The reason for such large variation is that, by nature, enamel composition and crystalline quality is different amongst people of different ages, races,

social background, etc. Moreover, different teeth in the same oral cavity may be exposed to different acidic and bacterial environments leading to variations in physical properties. Such variation is the nature of the tooth [46]. The same trend can be observed for the thermal properties of enamel as shown in Table 2.2.

Table 2.2 Thermal properties of sound enamel [45].

Thermal Conductivity (W $m^{-1}K^{-1}$)	Thermal diffusivity (m^2 s^{-1})
0.65 – 1.07	2.27×10^{-7} – 4.7×10^{-7}

2.6 Existing Optics-based early caries detection technologies

As mentioned earlier, existing clinical caries inspection methods such as X-ray radiography and visual/tactile assessment lack the sufficient sensitivity and specificity to detect early caries [38]. As such, a number of new technologies are currently under development to address the need for sensitive and reliable detection of caries at early stages of formation. Among these technologies, optical diagnostic methods have shown great potential as they utilize the intrinsic difference between optical properties (e.g., absorption or scattering) of the sound and demineralized tissues as the source of diagnostic contrast. Fiber-optic transillumination (FOTI) [47] is one such imaging method which uses high intensity white light for detecting caries. However, significant scattering of light in the visible spectrum as well as the masking effect of background signal originating from the healthy tissue surrounding the malignancy leads to relatively poor sensitivity and inconsistent results for FOTI [47]. Working on similar physical principles, near-infrared (NIR)

transmission/reflectance methods use near-infrared light instead of visible light to gain deeper penetration in dental hard tissues as a result of reduced scattering and absorption of enamel in the NIR region. However, poor detection specificity to early demineralization has been reported for these technologies mainly due to reliance of the diagnostic contrast on enhanced light scattering within the caries sites which can effectively be masked by the light scattering of the surrounding intact tissues and the anisotropic structure of dentin [44].

Optical coherence tomography (OCT) is another promising modality capable of imaging the tissue microstructure within the caries lesions. OCT works based on coherent collection of NIR backscattered light from an illuminated focal volume within the tissue and the analysis of the light intensity as it interfered with a reference light beam [32]. The intensity of the interference is dependent upon the degree of scattering caused by structural changes in the dental tissue [48]. Fried et al. [32] have demonstrated the application of a modified OCT system capable of producing polarization-sensitive OCT images to monitor caries lesion progression *in vitro*. Although promising results have been reported from this study, due to the relatively slow imaging speed of the OCT technology for interrogation of large fields of view, only isolated cross sectional (B-scan) images were reported rather than diagnostic images of the whole tooth. Several other studies have also been conducted to demonstrate the ability of OCT in detection of demineralization in enamel [49]. However, factors such as, formation of image artifacts as a result of interfering effect of intact tissues surrounding the malignancies with the backscattered light from caries, loss of coherence for deep zone imaging due to high light scattering, low imaging speed for inspection of

entire tooth surface, and high equipment cost limit the clinical adaptation of dental OCT [50].

Another category of optical diagnostic methodologies is known as the energy conversion technologies which operate based on transformation of optical energy to other energy forms. Quantitative light-induced fluorescence (QLF) is one such method which uses light-to-fluorescence conversion and the decrease in fluorescence transmission due to increased scattering from demineralized spots as a source of contrast. In QLF, fluorescence is caused by the excitation of fluorophores contained within the enamel-dentin junction using visible light. Although, QLF is capable of detecting early carious lesions [51], its sensitivity to masking effects of surface stains as well as the need for extensive operator training hinder the applicability of this technique in most real-life clinical scenarios [49].

Thermophotonic lock-in (TPLI) imaging is an alternative imaging modality which has recently been proposed for early dental caries detection [28]. This hybrid caries detection technology belongs to the group of energy conversion methodologies, where the excitation and detection channels are separated (i.e., optical excitation and thermal detection). In this imaging modality the crosstalk between the two channels occurs at caries sites as a result of enhanced local optical absorption within caries lesions [52]. This method has demonstrated an improved sensitivity to early caries compared to other conventional modalities as the masking background signal from healthy tissues surrounding the malignancies is suppressed due to selective absorption of light within early caries. TPLI is based on detection of the thermal infrared (Planck) radiation from caries and uses diffusive thermal waves as markers to gather information about subsurface caries.

In this method, a low-power, continuous, and intensity-modulated light source is utilized to generate a thermal wave field inside the tooth and the subsequent infrared emission of the thermal wave field is captured using an IR camera [28]. The temporal surface temperature modulation is evaluated and averaged over a number of cycles while the heat is generated in the sample periodically at a certain lock-in frequency. The role of lock-in modulation is to only evaluate the alternating (ac) part of the detected signal which carries information from subsurface inhomogeneities [28]. That is, subsurface defects alter the local centroid of the thermal wave field, leading to a phase delay as well as a change in the amplitude of the ac radiometric detected signal by the IR camera. As such, lock-in demodulation of the thermophotonic signals lead to calculation of phase and amplitude images with respect to the reference signal (i.e., optical excitation modulation signal) [28].

Chapter 3

Materials, Instrumentation, and Methods

In this chapter, the details of instrumentation and the experimental setup are explained. The data acquisition and signal processing program developed in the LabView environment along with the lock-in signal processing and synchronous undersampling algorithms which are implemented in the program are discussed. Finally, the preparation and characteristics of a series of standard non-biological and dental samples are provided.

3.1 Experimental Setup

Figure 3.1(a) depicts a schematic of the LWIR TPLI system used in this study. The setup consists of a multimode fiber coupled (core diameter = 200 μm) continuous wave near-infrared laser (808 nm; Jenoptik, Jena, Germany). A laser controller unit (Ostech, Berlin, Germany) is used to thermally stabilize the laser and to modulate its intensity. In order to have an illumination beam with uniform optical intensity over the interrogated area of the sample, a collimator (Thorlabs, Newton, New Jersey, USA, F220SMA-780) in conjunction with an optical diffuser (Thorlabs, Newton, New Jersey, USA, ED1-C20-MD) is used.

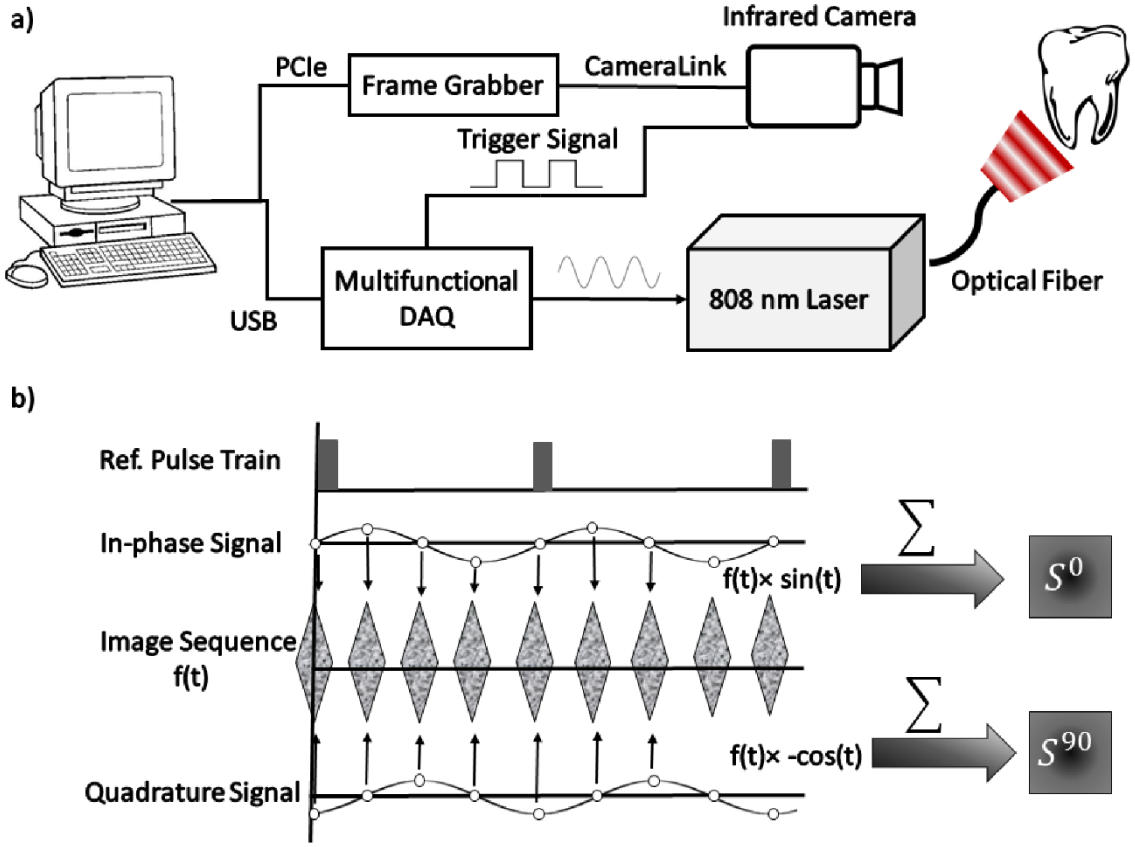

Figure 3.1 (a) The experimental setup consisting of a NIR laser, an LWIR camera, a frame grabber, and a multifunctional DAQ device. (b) Signal processing algorithm

A low-cost (~USD $6k) LWIR camera (Xenics, Leuven, Belgium) with Cameralink communication protocol standard, spectral range of 8-14 μm, and maximum frame rate of 50 fps is focused on the surface of a LEGO-mounted sample. The sample is placed on a rotation stage mounted on a three-axis XYZ translation stage (precision 10 μm). An 18 mm focal-length objective lens (Xenics OPT-000179) along with a custom made extension tube is installed on the camera to obtain a magnification of unity (1) from the interrogated surface of the sample. LWIR camera frames are acquired by a frame grabber (Euresys,

Angleur, Belgium, Grablink Full). A multifunctional data acquisition board (National Instruments, Austin, Texas, NI USB-6363 BNC) synchronously generates three analog signals: reference pulse train, in-phase, and quadrature reference signals. The laser controller modulates the intensity of the laser beam using the in-phase reference signal.

The lock-in demodulation algorithm (Figure 3.1(b)) is implemented in a computer program, designed in LabView environment, which captures the images at a specified frame rate and at the same time records the corresponding values of in-phase and quadrature signals as well as the reference pulse train status (high or low).The program captures an image sequence and finds the beginning of a modulation cycle using the pulse train information and uses the reference signal values to calculate the weighted average of an image sequence corresponding to an integer multiple of lock-in modulation period using the instantaneous readings of the two reference signals. Subsequently, the weighted frames are summed to obtain in-phase (S^0) and quadrature (S^{90}) images. Equation 3.1 depicts the mathematical analogue of this signal processing algorithm in which the sinusoidal signals are first written in expanded form and then by applying the low-pass filter the amplitude and phase of the detected signal are calculated.

$$\begin{cases} \sin(\omega_o t)\times A\sin(\omega_o t+\phi) \\ \sin(\omega_o t+90)\times A\sin(\omega_o t+\phi) \end{cases} \xrightarrow{Mixing} \begin{cases} \frac{A}{2}\left[\cos(\phi)-\cos(2\omega_o t+\phi)\right] \\ \frac{A}{2}\left[\sin(\phi)-\cos(2\omega_o t+\phi+90)\right] \end{cases} \xrightarrow{Weighting \times\sqrt{2}}$$

$$\begin{cases} \frac{A}{\sqrt{2}}\left[\cos(\phi)-\cos(2\omega_o t+\phi)\right] \\ \frac{A}{\sqrt{2}}\left[\sin(\phi)-\cos(2\omega_o t+\phi+90)\right] \end{cases} \xrightarrow{LPF} \begin{cases} S^0=\frac{A}{\sqrt{2}}\cos(\phi) \\ S^{90}=\frac{A}{\sqrt{2}}\sin(\phi) \end{cases} \rightarrow \begin{cases} A=\sqrt{(S^0)^2+(S^{90})^2} \\ \phi=\arctan\left(\frac{S^{90}}{S^0}\right) \end{cases} \quad (3.1)$$

here $\sin(\omega_o t)$ and $\sin(\omega_o t + 90)$ represent the in-phase and quadrature reference signals and $A\sin(\omega_o t + \phi)$ is the captured infrared signal with amplitude A and phase ϕ.

The signal processing steps usually take a few seconds. Therefore, the experiment time strongly depends on the duration of the modulation cycle (i.e. lock-in frequency) as well as the signal-to-noise ratio (SNR) of the acquired signals (i.e. number of required averaging). SNR is a measure that compares the level of a desired signal to the level of background noise and is defined as the ratio of signal power to the noise power. The higher the laser intensity, the lesser the number of required averaging to get an acceptable SNR.

3.2 Synchronous undersampling

One of the limitations of inexpensive infrared cameras is the low frame rate (e.g., maximum of 50 Hz for the LWIR camera used in this study), limiting their ability to monitor high frequency phenomena. Theoretically, to retrieve the amplitude and phase information of signals a minimum of n=4 samples per modulation cycle are to be obtained [53]; however, oversampling of typically n=10 is often employed in practice to achieve acceptable signal-to-noise ratio. To overcome the acquisition speed limitation in our LWIR TPLI system, for modulation frequencies above 5Hz the LabView data acquisition program automatically runs a subroutine based on the synchronous undersampling algorithm in which the required "n" samples per modulation cycle are captured from "n" consecutive cycles instead of one [53]. Using this method, the developed system can reliably interrogate dental samples at photothermal modulation frequencies of up to 1kHz. Figure 3.2 graphically explains how 12 consecutive cycles can be used to sample one modulation cycle with 12 points.

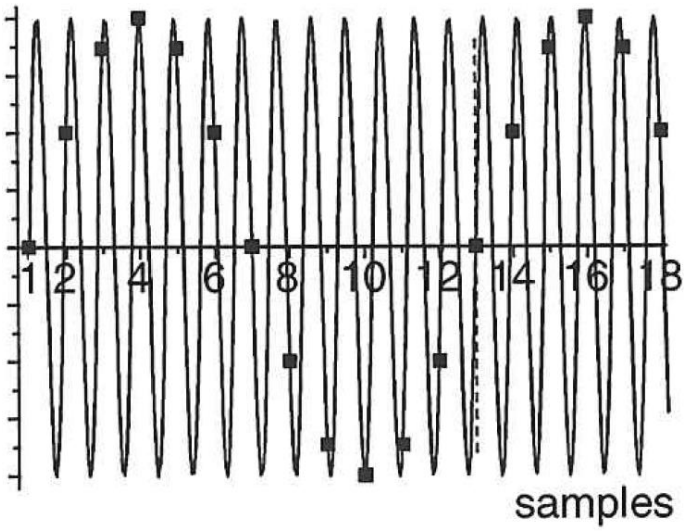

Figure 3.2 Synchronous undersampling of a high frequency wave form using a low sampling rate. One modulation cycle is sampled out of each 12 consecutive cycles [53]

Equation 3.2 shows the relationship between the modulation frequency, *f*, and the synchronous undersampling frequency, f_s [53].

$$f_s = f(1 - \frac{1}{n}) \tag{3.2}$$

3.3 Samples

3.3.1 Standard Opaque Sample

To evaluate the capabilities of the imaging system, a number of biological and non-biological samples are used in this study. An aluminum block with three 5-mm diameter blind holes, located at various depths from the surface, was prepared to simulate an opaque sample with defects at several depths. The holes were drilled to give wall thicknesses of 200 μm, 500 μm, and 1500 μm (shown in figure 3.3). The interrogated side of the sample is painted with a matt black color to enhance the optical absorption on the surface.

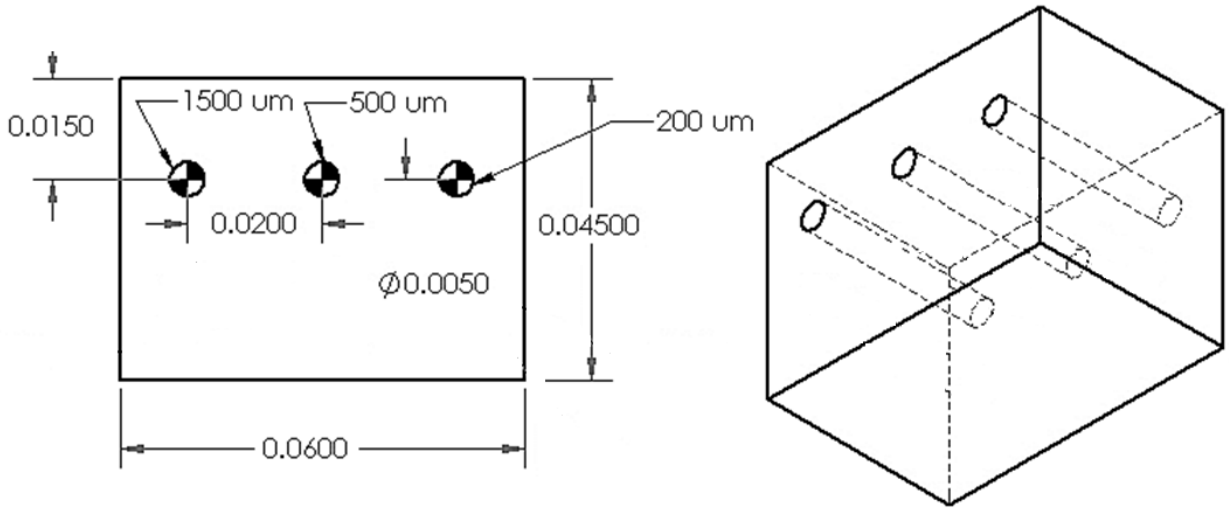

Figure 3.3 Opaque standard sample with three holes.

3.3.2 Dental Samples

In this thesis, the diagnostic performance of the LWIR imaging system is evaluated through artificial demineralization of dental samples. Extracted human teeth were obtained from local dental offices and teeth with no visible stains or white spot lesions, were selected for the study. After preliminary visual inspection, the samples were cleaned and mounted on LEGO blocks using an epoxy adhesive. This allows the samples to be remounted in the same position in the experimental setup during repeated measurements.

3.3.3 Controlled Demineralization Protocol

A widely used lactic acid-based solution [28, 30, 54] was applied on dental samples to induce controlled demineralization. The solution was an acidified gel, consisting of 0.1 M lactic acid and 0.1 M NaOH, gelled to a thick consistency with addition of 6% w/v hydroxyethylcellulose. To produce the solution, free Lactic acid is to be used which is a

liquid with a molecular weight of 90.1, specific gravity of 1.249, containing 85% Lactic acid by weight. The Lactic acid should be diluted with deionized water to from a 0.1 M solution by pipetting 4.243 ml of Lactic acid and 500ml of de-ionized distilled water into a beaker and mixing the two together with the aid of a magnetic stirrer. Then 2.0g of NaOH is to be measured out using the electronic weighting scale and dissolved in 500ml of de-ionized distilled water. In the next step, pH meter electrode was inserted into the 0.1M Lactic acid solution to verify a pH level of 2.5. The 0.1M NaOH was gradually added into the 0.1M Lactic acid with a continued stirring using a magnetic stirrer. The variation in pH was beingnoted in pH meter until the pH of the solution became 4.5. Approximately 500ml of 0.1M NaOH should be used. To begin the gelation process, 500ml of the acid buffer solution produced was retained and 30g of 6%(W/V) hydroxyethyl cellulose (HEC) was measured out and added to the solution. The HEC was added slowly with continued stirring using a kitchen mixer. As the stirring continued the viscosity of the solution was increased. Stirring was continued until the consistently had reached to the level point that if one brings it up with a spatula it cannot easily drop. After formation of the gel, 20ml was poured into each universal container containing the tooth. The sample was rotated after 24 hours to eliminate air bubbles especially those on the treatment window on the enamel surface.

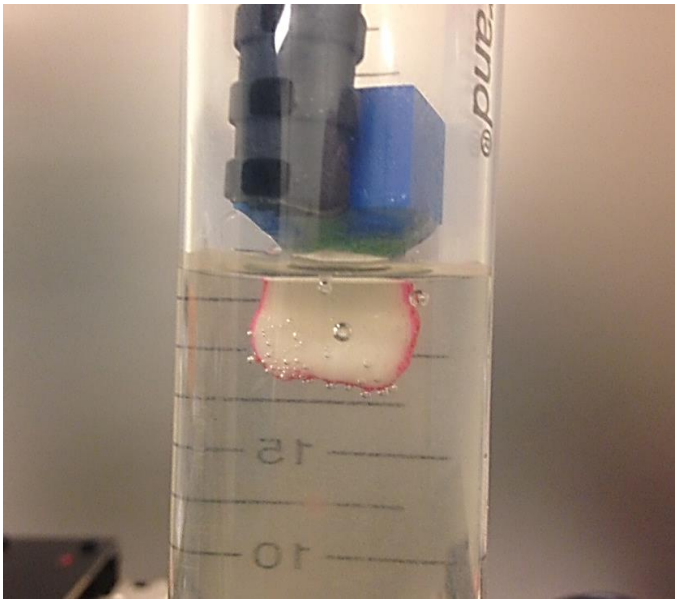

Figure 3.4 Submerged dental sample in the acidic gel

The aim of controlled demineralization in this thesis is to observe the contrast between demineralized and healthy areas during different stages of caries formation. To this end, a treatment protocol was followed in time-dependent experiments in which the tooth surface was covered with an acid-resistant transparent nail polish except for a 2.5 mm (W) × 5 mm (H) rectangular window (i.e., treatment window). The demineralization on the window was carried out by submerging the sample in a test tube containing 20 ml of demineralizing gel. The treatment was repeated in four- and six-hour and as well as two-day intervals for the detection threshold and controlled demineralization studies, respectively. After each treatment, the sample was removed from the gel, cleaned by rinsing under running water, and dried in air. Then, the transparent nail polish was removed from the interrogated surface with nail polish remover and the sample was again rinsed and air dried before TPLI. In addition, a photograph of the sample was taken using a high magnification CCD camera

at each demineralization step to monitor the appearance of the white spot lesion. After imaging, the sample was again covered with the transparent nail polish (except for the treatment window) and demineralized for an additional treatment interval in order to investigate the progression of demineralization. The treatment window of samples used in this study were demineralized for up to 10 days. Thermophotonic imaging was carried out on samples before treatment as well as after each treatment step. Several studies carried out using gold standard methods such as transverse micro-radiography (TMR) have verified the ability of this demineralization protocol in producing a subsurface lesion in enamel with a sound surface layer (i.e., the characteristic mineral profile of early dental caries) [30, 45, 55-57].

Chapter 4

Theoretical Modelling

In this chapter, a comparison has been made between the diagnostic performance for caries detection in the LWIR with the MWIR bands. Through theoretical calculation of the radiometric signal detected by the infrared camera, the phase and amplitude values of the signal for caries located at different depths inside the tissue have been studied. Accordingly, the diagnostic contrast in LWIR detection has been compared to that of MWIR band.

4.1 Theory

The light-matter interaction in turbid media (e.g., dental hard tissues) is governed by strongly coupled diffused-photon-density and thermal-wave processes [58]. In the case of dental caries, the enhanced local optical scattering and absorption at caries results in generation of strong subsurface thermal-wave sources, contributing to the infrared detector signal radiometrically in the form of the following depth-integrated formula [58]:

$$S(l;t) \propto \bar{\mu}_{IR} \int_0^l T(z,t) \exp(-\bar{\mu}_{IR} z)\, dz \qquad (4.1)$$

here $\bar{\mu}_{IR}$, l, and $T(z,t)$ are the average infrared absorption coefficient over the detection wavelength bandwidth (MWIR: 3-5µm, LWIR: 8-14 µm), caries/absorber depth, and the induced thermal-wave field, respectively.

Equation 4.1 suggests that the radiometric signal registered by the IR detector gets contributions from the thermal-wave field in the form of an exponentially attenuated depth-integral, with $\bar{\mu}_{IR}$ serving as the attenuation coefficient. Therefore, the spectral bandwidth

of the detector (MWIR vs. LWIR) plays an important role in the physical nature of the acquired IR signals. In the case of a MWIR TPLI system, the direct Plank emission (radiative heat transfer) from subsurface thermal sources (e.g., early caries) dominates the conductive thermal-wave contribution from the interrogation surface as a result of relatively low $\bar{\mu}_{IR}$ (enamel transmittance: MWIR=75% [44]) in this spectral region. Such dominant radiative contribution from subsurface thermal sources in the MWIR band is carried out at the speed of light (i.e., no delay), masking the desirable delayed conductive thermal-wave contribution required for generating diagnostic contrast in dental TPLI images. In contrast to MWIR band, $\bar{\mu}_{IR}$ is significantly large within LWIR band (enamel transmittance: LWIR=7% [44]) which effectively results in attenuation of the instantaneous radiative contribution from the subsurface thermal sources, allowing for reliable detection of delayed thermal-wave contributions emanating from the sample surface which carry the desired diagnostic information.

To demonstrate the advantages of LWIR TPLI in detection of subsurface absorbers in turbid media, thermophotonic signals from thermal sources located at different depths are theoretically modelled and the LWIR TPLI and MWIR TPLI responses are compared. That is, the thermophotonic response (Planck radiation emission) of a turbid medium subjected to an amplitude-modulated optical excitation is calculated by solving the associated coupled diffuse-photon-density and thermal-wave field boundary value problem, as a simplified model of the real-life problem (i.e., dental caries detection). Subsequently, the response of black body absorbers (i.e., defects/early caries) located at different depths inside a turbid medium with known scattering and absorption coefficients (μ_s and μ_a,

respectively), is analytically derived. The frequency-domain thermal-wave problem can be formulated by considering a depth dependent source term (i.e. attenuated energy fluence of a beam $I(z)$ [59]) for the heat diffusion differential equation as well as a thermal source (e.g. early caries) at $z=L$ through the boundary condition (Equation 4.2).

$$\begin{cases} \frac{\partial^2\theta(z;\omega)}{\partial z^2} - \sigma^2\theta(z;w) = -\frac{\mu_a}{k} I(z)F(\omega) \\ -k\frac{\partial\theta(z;\omega)}{\partial z}\Big|_{z=0} = 0 \\ -k\frac{\partial\theta(z;\omega)}{\partial z}\Big|_{z=l} = I(l)F(\omega) \\ \theta(z;\omega) = \Im\{T(z,t) - T_\infty\} \end{cases} \tag{4.2}$$

here k, T_∞, and $F(\omega)$ are thermal conductivity, sample equilibrium temperature, and the spectrum of the applied optical excitation, respectively. $\Im$ denotes the Fourier transform operator and $\sigma = \sqrt{\frac{i\omega}{\alpha}}$ is the complex wavenumber, where ω and α are laser modulation frequency and thermal diffusivity, respectively.

$I(z)$is the energy fluence of the one-dimensional, uniform, collimated beam incident on a homogeneous scattering and absorbing medium [60] and can be expressed as:

$$I(z) = \beta\exp\left(-\mu_{eff}\, z\right) + \gamma\exp\left(-\mu_t z\right)$$
$$\beta = \left[\frac{I_o(9+6w)\mu_s' D}{\left(1+w\sqrt{4\mu_a D}\right)\left(1-9\mu_a D\right)}\right] \quad \textit{and} \quad \gamma = \left[\frac{-2I_o}{1-9\mu_a D}\right] \tag{4.3}$$

where $\mu_{eff} = \sqrt{3\mu_a\mu_t}$, $\mu_t = \mu_a + \mu_s'$, $\mu_s' = \mu_s(1-g)$, $D = (3\mu_t)^{-1}$, $w = (1+r)/(1-r)$, I_o, g, and r are optical fluence on sample surface ($z = 0$), the average cosine of the scattering angle, and the internal diffuse reflection coefficient, respectively. Equation 4.2

is an ordinary nonhomogeneous differential equation whose solution can be found through summation of its general and particular solutions, $y = y_p + y_c$.

$$\begin{aligned} y_c &: \ \theta(z;\omega) = A\exp(\sigma z) + B\exp(-\sigma z) \\ y_p &: \ \theta(z;\omega) = C\exp(-\mu_{eff} z) + D\exp(-\mu_t z) \end{aligned} \tag{4.4}$$

By inserting y_p into equation 4.2 we get:

$$C = \frac{\mu_a \beta F(\omega)}{\kappa\left(\sigma^2 - \mu_{eff}^{\ 2}\right)} \qquad D = \frac{\mu_a \gamma F(\omega)}{\kappa\left(\sigma^2 - \mu_t^{\ 2}\right)} \tag{4.5}$$

By applying the first boundary condition, we get:

$$B = A - \frac{\mu_{eff} C}{\sigma} - \frac{\mu_t D}{\sigma} \tag{4.6}$$

Applying the second boundary condition we get:

$$A = \frac{C\mu_{eff}\left[\exp\left(-\mu_{eff} l\right) - \exp\left(-\sigma l\right)\right] + D\mu_t\left[\exp\left(-\mu_t l\right) - \exp\left(-\sigma l\right)\right] - \frac{I(l)}{\kappa} F(\omega)}{\sigma\left[\exp\left(\sigma l\right) - \exp\left(-\sigma l\right)\right]} \tag{4.7}$$

Consequently, the spectrum of radiometric signal can be calculated as:

$$S_c(l;\omega) \propto \bar{\mu}_{IR} \int_0^l \theta(z,\omega) \exp(-\bar{\mu}_{IR} z)\, dz \tag{4.8}$$

$$= \bar{\mu}_{IR} \left[\frac{A}{\sigma - \bar{\mu}_{IR}} (\exp[(\sigma - \bar{\mu}_{IR})l] - 1) - \frac{B}{\sigma + \bar{\mu}_{IR}} (\exp[-(\sigma + \bar{\mu}_{IR})l] - 1) \right.$$

$$- \frac{C}{\mu_{eff} + \bar{\mu}_{IR}} \left(\exp\left[-\left(\mu_{eff} + \bar{\mu}_{IR}\right)l\right] - 1\right)$$

$$\left. - \frac{D}{\mu_t + \bar{\mu}_{IR}} (\exp[-(\mu_t + \bar{\mu}_{IR})l] - 1) \right]$$

where $\mu_{eff} = \sqrt{3\mu_a\mu_t}$, $\mu_t = \mu_a + \mu_s'$, $\mu_s' = \mu_s(1-g)$, g is the average cosine of the scattering angle. In this thesis the absorption coefficient, scattering coefficient, thermal conductivity, and thermal diffusivity are chosen, based on the properties of dental enamel, to be 100 m^{-1}, 6000 m^{-1}, 0.9 $Wm^{-1}k^{-1}$, and 5×10^{-7} m^2s^{-1}, respectively [52].

4.2 Theoretical modelling of caries detection in the MWIR and LWIR bands

The radiometric signal is calculated for two extreme values of infrared absorption coefficients ($\bar{\mu}_{IR}$), corresponding to the LWIR and MWIR spectral bands (i.e., 100 (MWIR) and 50000 (LWIR) m^{-1}) with three different absorber depths (100, 500, and 900 µm) considering a 2 Hz photothermal modulation frequency. The modelled lock-in amplitude values for absorbers located at 100, 500, and 900 µm below the interrogation surface for the MWIR and LWIR detection bands are shown in figures 4.1(a) and 4.1(b), respectively. The normalized amplitude values suggest that for MWIR detection (small $\bar{\mu}_{IR}$), the amplitude of the signal exhibits poor sensitivity to absorber depth as a result of

low absorption of direct thermal radiation by the medium and the consequent domination of the instantaneous direct Planck radiation over the delayed conductive thermal waves. On the other hand, in the case of LWIR detection (large $\bar{\mu}_{IR}$), the amplitude difference at various depths (i.e., detection sensitivity) becomes considerable as the instantaneous Planck infrared radiation is strongly absorbed by the medium surrounding the subsurface thermal sources, allowing for the proper detection of delayed conductive thermal waves.

The lock-in phase values for signals originated from absorbers at different depths is also modelled for both values of infrared absorption coefficients. As depicted in figures 4.1(c) and 4.1(d), a similar behavior to the amplitude values is observed in the phase channel. At MWIR detection band, the instantaneous contributions of the direct Planck emission from deep regions dominate the conductive thermal wave contributions. Consequently, there will be minimal contrast between defects located at different depths. On the contrary, the modelling results of LWIR band show a substantial phase difference between the signals originating from absorbers at different depths. The phase values demonstrate such trend due to the suppression of direct infrared (Planck) emission, allowing only the thermal waves that conductively reached the surface of the tooth to contribute to the camera signal.

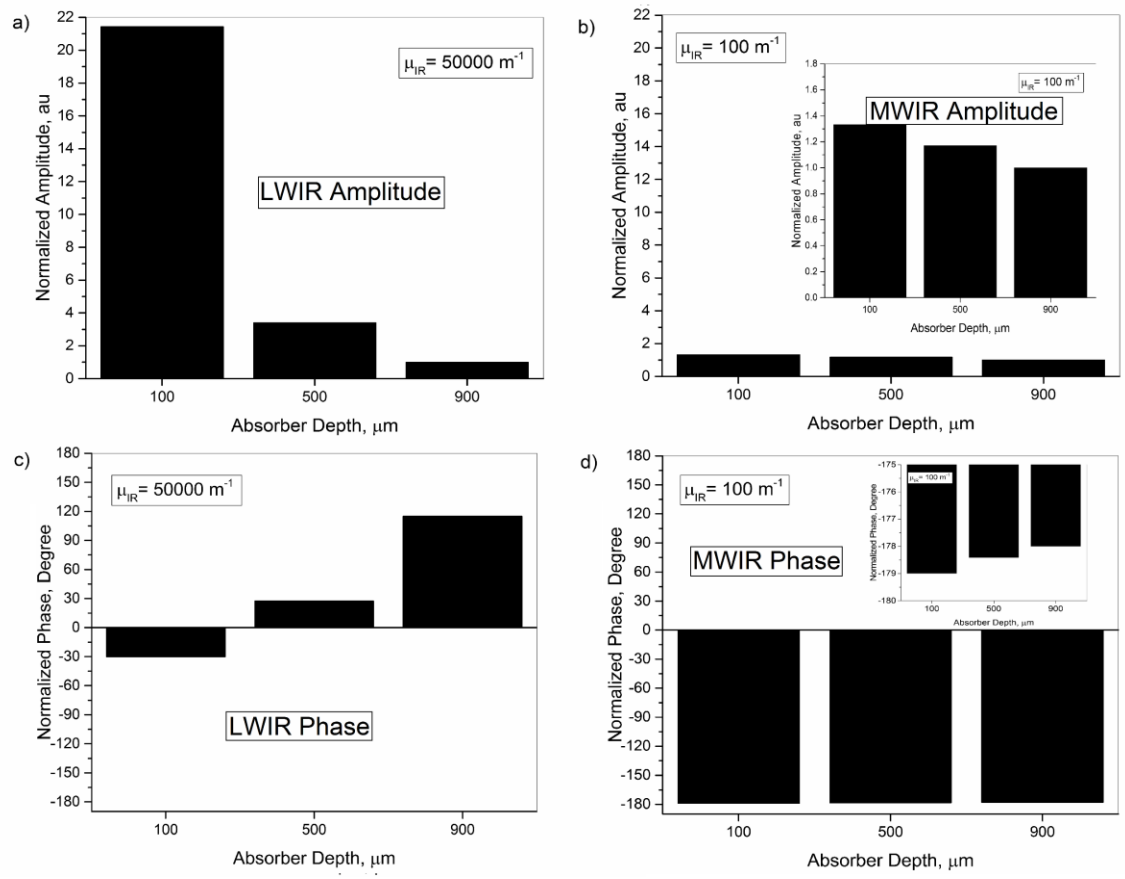

Figure 4.1 Phase and amplitude of the theoretical radiometric signal calculated for MWIR and LWIR detection spectral bands from absorbers located at different depths. Normalized amplitude values for (a) LWIR ($\bar{\mu}_{IR}$ =50000 m^{-1}) and (b) MWIR ($\bar{\mu}_{IR}$ =100 m^{-1}). Normalized phase values for (c) LWIR ($\bar{\mu}_{IR}$ =50000 m^{-1}) and (d) MWIR ($\bar{\mu}_{IR}$ =100 m^{-1})

To further extend the findings from theoretical modelling the phase and amplitude of the signal are calculated for seven different values for $\bar{\mu}_{IR}$, chosen in an increasing order (100, 300, 800, 1500, 2000, 4000, 50000 m^{-1}), to simulate the effect of medium infrared absorption coefficients on the radiometric signal. The signal phase and amplitude values are plotted over a variety of absorber depths (0 to1000 μm) where caries formation is more likely to occur (Figures 4.2 and 4.3). The results indicate that by increasing the absorption

coefficient, the phase values at different absorber depths become more distinct (i.e., better detection sensitivity) which leads to higher contrast between the phase images obtained from features located at different depths in the turbid medium.

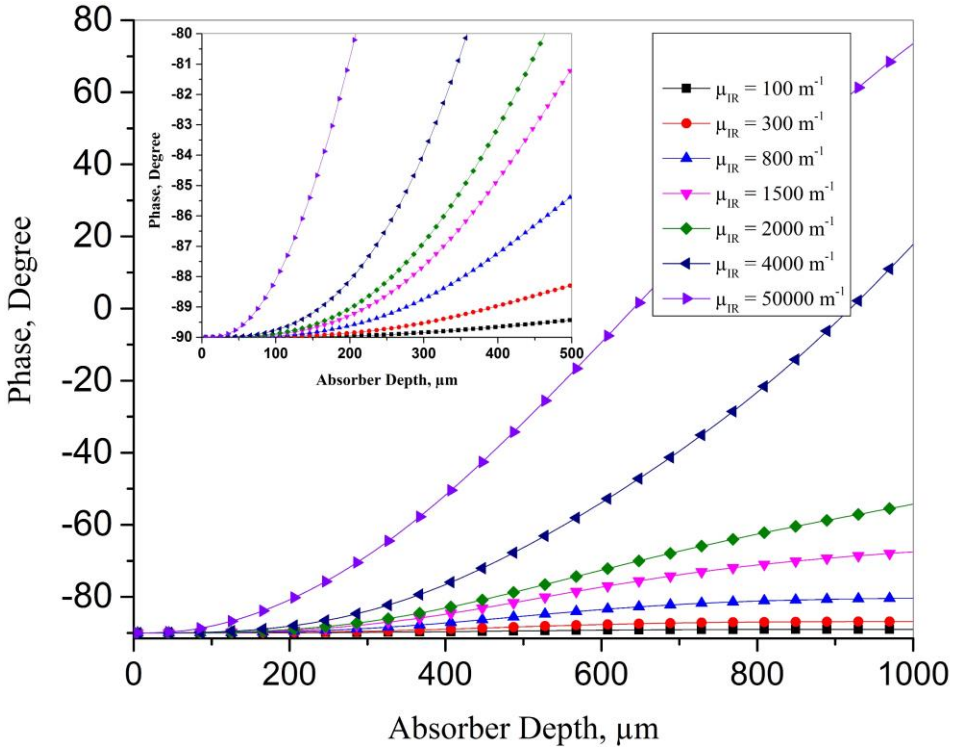

Figure 4.2 Theoretical radiometric signal phase vs. absorber depth for several μ_{IR} values

Figure 4.3 shows that at a given absorber depth, the amplitude increases with increasing medium infrared absorption coefficient due to the proportionality of the radiometric signal to $\bar{\mu}_{IR}$ (Equation 4.1), resulting in a signal with higher SNR Moreover, at small values of the medium infrared absorption coefficient, the detection sensitivity is significantly reduced such that the amplitude is independent of the absorber depth.

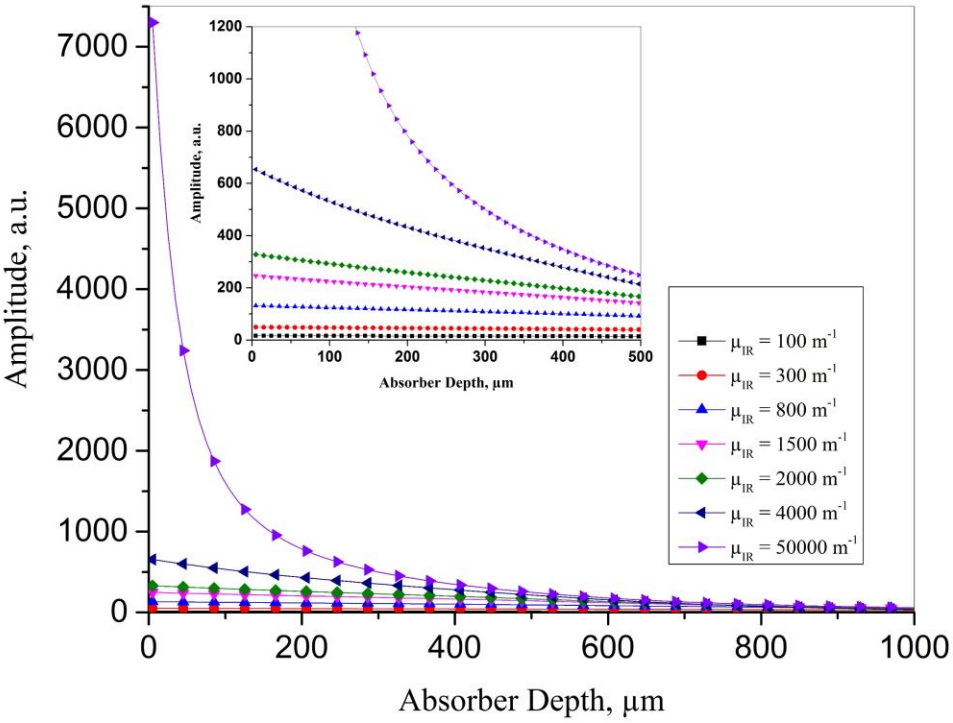

Figure 4.3 Theoretical radiometric signal amplitude vs. absorber depth for several μ_{IR} values

The obtained results from theoretical modelling demonstrate that LWIR detection yields better diagnostic contrast and detection sensitivity in thermophotonic imaging (TPI) of dental hard tissues than the existing caries detection technology in the MWIR band. Furthermore, from the thermal-wave science point of view, radiometric interrogation of enamel in the LWIR band is advantageous as the direct Plank emission (radiative heat transfer) from subsurface regions is effectively suppressed due to the minimal optical transmittance of enamel (enamel transmittance: MWIR=75%, LWIR=7% [44]), allowing the registration of pure conductive thermal waves by the camera which carry the diagnostic information [59].

Chapter 5
Thermophotonic Lock-in Imaging

This chapter starts with a short review of the thermal-wave principles followed by a discussion on the TPLI of a standard opaque sample. After validating the capabilities of the developed system in imaging of subsurface defects in the standard sample, thermophotonic imaging of artificially-induced proximal and occlusal caries are discussed in detail. Afterwards, the abilities of the system in detection of natural occlusal caries are demonstrated and the sensitivity threshold of system to detect very early demineralization in dental hard tissues is investigated.

5.1 Basic principles of thermal-waves

As discussed in the first chapter, photothermal radiometry uses thermal waves as markers to gain information about subsurface features in materials. Following the absorption of a modulated excitation in PTR, a diffusive thermal field is formed inside the medium. This periodically oscillating temperature field resembles a wave field and is therefore referred to as the thermal-wave field. However, unlike hyperbolic travelling waves such as acoustic or optical waves, physics of the formed diffusive thermal waves are governed by the parabolic differential equation (i.e., heat diffusion equation). Thermal wave field in a solid is a scalar field determined by the thermal diffusion equation and can be formulated as:

$$\nabla^2 T(x,y,z,t) - \frac{1}{\alpha}\frac{\partial T(x,y,z,t)}{\partial t} = -\frac{H(x,y,z,t)}{\kappa} \qquad (5.1)$$

Here T (x,y,z,t) is the excess temperature at point (x,y,z) at time t relative to a reference ambient temperature T_o, H(x,y,z,t) is the source term and is the rate of heat input per unit volume, α [m^2/s] is thermal diffusivity, and κ [W/(m.K)] is thermal conductivity. For partial differential equations involving modulated heat generation source term, it is more convenient to solve the problem in frequency domain:

$$\nabla^2\theta(x,y,z,\omega)-\sigma^2\theta(x,y,z,\omega)=-\frac{\tilde{H}(x,y,z,\omega)}{\kappa} \tag{5.2}$$

$$\sigma=\sqrt{\frac{i\omega}{\alpha}}=\frac{1}{\mu}(1+i) \tag{5.3}$$

where θ (x,y,z,ω) and $\tilde{H}(x,y,z,\omega)$ are the frequency domain counterparts of T and H, mathematically obtained through temporal Fourier transform. σ is the complex wavenumber and μ is the thermal diffusion length defined as:

$$\mu=\sqrt{\alpha/\pi f}=\sqrt{2\alpha/\omega} \tag{5.4}$$

Here α, f, and ω are the sample thermal diffusivity, the optical excitation modulation frequency, and the optical excitation modulation angular frequency, respectively.

Many important properties of thermal waves can be inferred from the abovementioned equations. Equation 5.2 is very similar to the Helmholtz equation of hyperbolic wave-fields; however, the complex character of σ and the gradient driven nature of heat diffusion do not allow the generation of hyperbolic waves, resulting in the lack of wave fronts and the diffuse depth-integrated (rather than localized) nature of thermal waves. An immediate consequence of the gradient-driven principle and the depth-integrated transport of power

through the medium in the diffusive thermal wave field is the poor diffusive axial resolution.

To simplify equation 5.2, most of the photothermal radiometry techniques incorporate an expanded beam excitation where the excitation source covers an area on the sample that is much larger than the thermal diffusion length. In such cases, the heat diffusion equation used for characterizing the thermal-wave field inside the medium becomes planar and as such the three dimensional equation is reduced to a one dimensional problem.

$$\frac{\partial^2}{\partial z^2}\theta(z,\omega) - \sigma^2\theta(z,\omega) = -\frac{\tilde{H}(z,\omega)}{\kappa} \tag{5.5}$$

To obtain a better understanding of the principles of thermal-waves, let's consider an opaque homogeneous semi-infinite medium (e.g. a thick steel block) whose surface is subjected to plane periodic heating of the form $(I_o/2)[1+\cos(\omega t)]$. Solution of the frequency-domain problem and transforming back to time-domain using inverse Fourier transform yields the equation of thermal-waves for this geometry:

$$T(z,t) = \frac{Q_o}{2\sqrt{2}\kappa}\mu\exp(-\sigma z)\exp\left[i\left(\omega t - \frac{\pi}{4}\right)\right] \tag{5.6}$$

Careful inspection of equation 5.6 reveals that, for a given sample and at a given laser modulation frequency (ω), the thermal waves are exponentially dissipated as they travel within the medium because the term "exp(-σz)" acts as a spatial damping function. As such, thermal diffusion length (μ in equation 5.4) is defined as the depth at which the thermal wave amplitude is reduced to e^{-1} of its initial value. Moreover, the damping constant (σ in

equation 5.3) is directly proportional to the modulation frequency (ω). This suggests that the low frequency thermal waves are less damped and enough time is given to them to propagate into the deep regions of the medium and can inspect deep into the sample, while the high frequency thermal waves are heavily damped and limited to the near the surface depths. Consequently, the inspection depth of photothermal systems can be adjusted by controlling the modulation frequency/thermal diffusion length.

5.2 Validation of the developed LWIR TPLI system

To obtain the theoretical radiometric signal for opaque materials in which light is absorbed within few microns of the interrogated surface (i.e.,$\bar{\mu}_{IR}$ is significantly large and can effectively be replaced with infinity) one can insert equation 5.6 into equation 4.1.

$$\xrightarrow[\text{Opaque material}]{\bar{\mu}_{IR}\to\infty} S(t,\omega)=\frac{Q_o}{2\sqrt{2}\kappa}\times\mu\times\exp\left[i\left(\omega t-\frac{\pi}{4}\right)\right] \tag{5.7}$$

Equation 5.7 denotes that for a semi-infinite opaque material, the amplitude of the radiometric signal is proportional to μ or alternatively proportional to $1/\sqrt{\omega}$ and, regardless of the modulation frequency (ω), the phase is always -45º. However, the presence of a defect below the surface violates the semi-infinite assumption and results in a higher photothermal amplitude as well as a photothermal phase value other than -45º.

To verify that the developed system follows the aforementioned basic principles of PTR, an aluminum block sample with blind holes was examined. The phase images of the blind holes (200, 500, and 1500 µm wall thicknesses) in the aluminum sample, obtained at 5, 10, and 20 Hz optical excitation modulation frequencies, were normalized with respect to the

average phase value calculated over an area with no defects and are presented in Figure 5.1. The sequence of images suggests that the developed LWIR system is capable of resolving holes at different depths with acceptable resolution. As expected, at a given modulation frequency, as the wall thickness increases the outline and the shape of the holes appear with a lower resolution due to the diffuse nature of heat conduction.

The depth profilometric nature of TPLI can also be understood by comparing phase images of figure 5.1. For a given defect depth, increasing the modulation frequency decreases the thermal diffusion length, leading to a lower effective detection depth and fading of the deeper holes. Consequently, while the intermediate defect (500 μm wall thicknesses) is present in the images at 5 Hz; it fades away by increasing the modulation frequency to 10 Hz and completely disappears at 20 Hz. The results of figure 5.1 demonstrate the basic principles of thermal-waves and serves as a fundamental validation of the developed LWIR TPLI system.

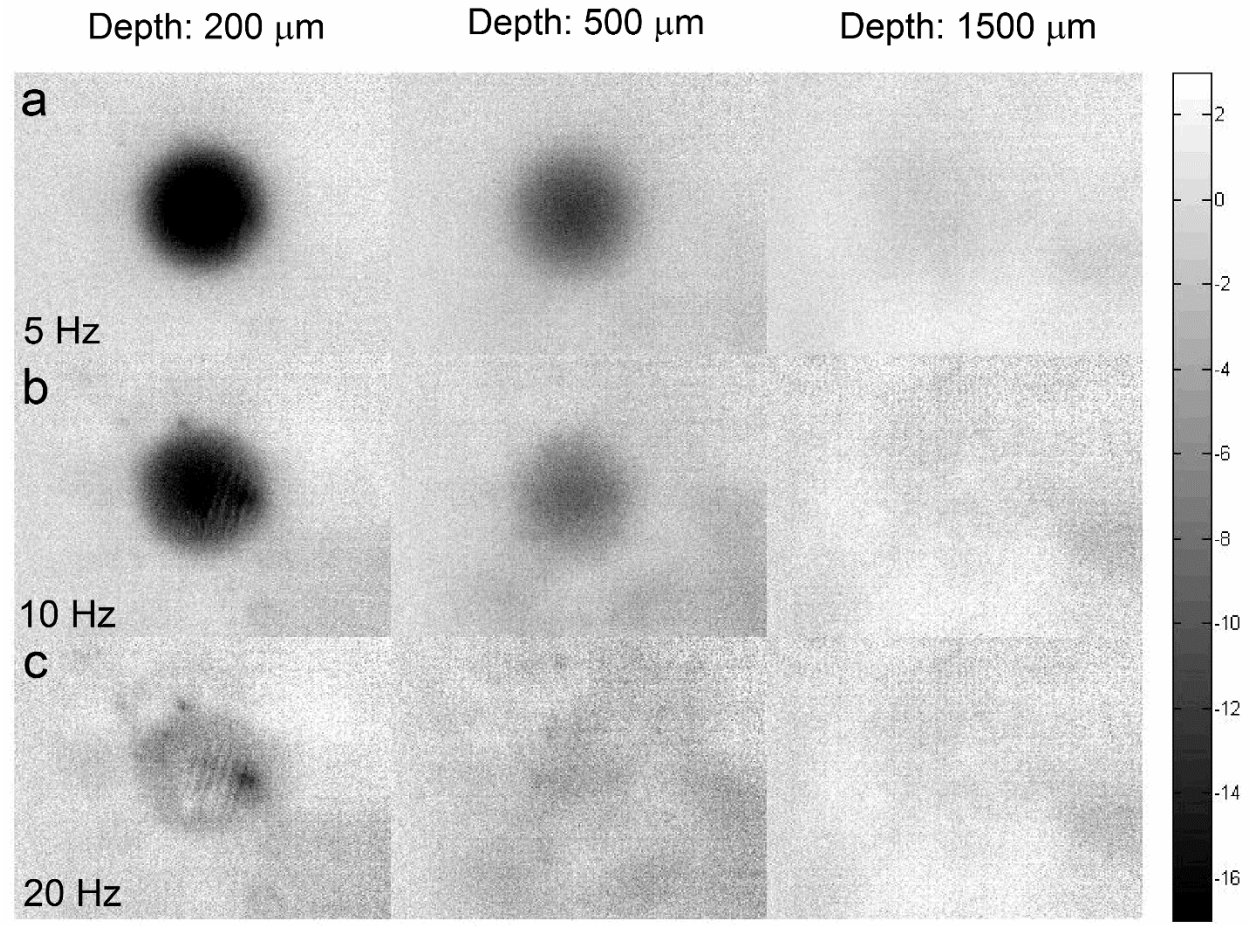

Figure 5.1 Normalized phase images of blind holes with different depths obtained at (a) 5 Hz, (b) 10 Hz, and (c) 20 Hz, respectively

5.3 Detection of dental caries

In this thesis, a systematic procedure is employed to investigate the progression of demineralization into the enamel over time. This procedure involves phase normalization [28] to ensure that the sequence of images taken at various stages of demineralization is self-consistent as the optical and thermal properties of teeth slightly change over time. As such, the pixel values of each TPLI image is normalized by average pixel value of an intact

reference area (e.g., dashed reference area in figure 5.2(c)). This normalization is the only modification made on the raw TPLI images in this thesis.

5.3.1 Detection of proximal caries

The visual photograph of the sample before demineralization is depicted in figure 5.2(a). The dashed rectangle indicates the interrogated surface of the sample in our TPI system while the solid rectangle shows the location of the treatment window. No dominant defect is visually observed in this sample. The normalized TPLI amplitude image obtained at 2 Hz modulation frequency before application of artificial demineralization (Figure 5.2(c)) also confirms this finding. As such, the sample deemed to be reasonably healthy before application of the demineralization protocol. The visual photograph of the sample after application of demineralization for 10 days is shown in figure 5.2(b). To acquire the photographs, the samples are air-blown and dried for 10 seconds to simulate the condition under which the visual inspection of caries is typically carried out in clinical scenarios.

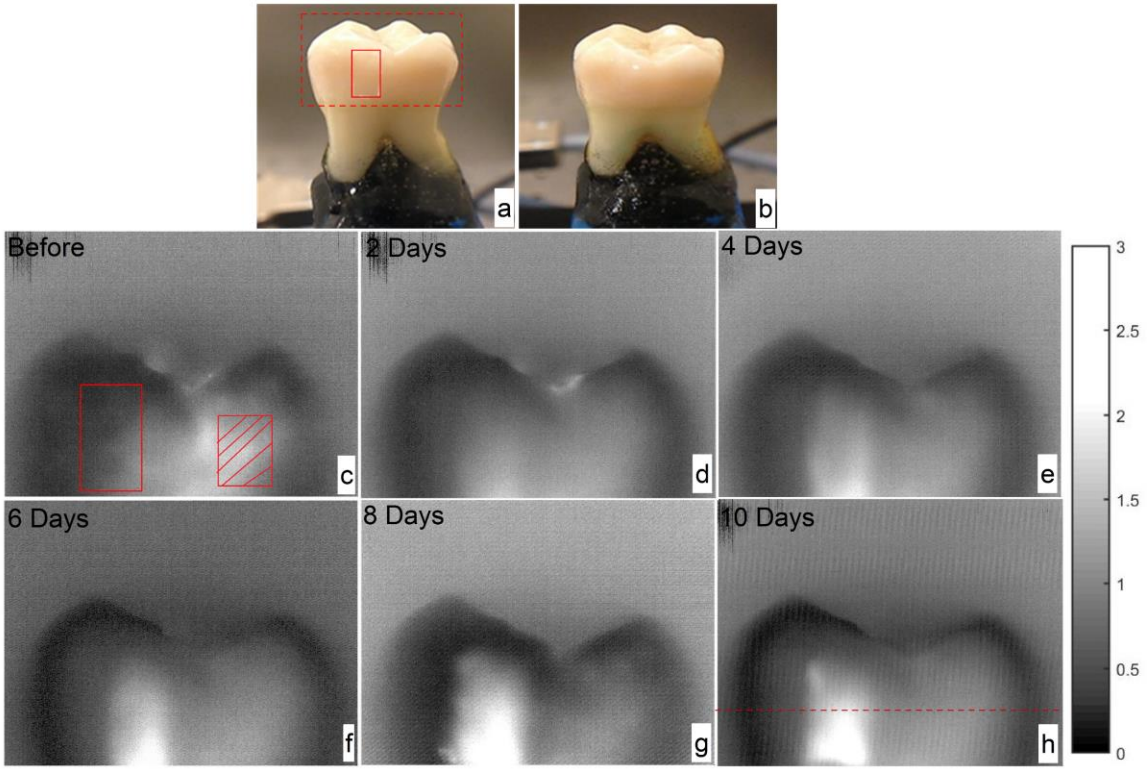

Figure 5.2 Optical image of the sample with proximal caries (a) before and (b) after 10 days of demineralization on the treatment window. Normalized TPLI amplitude images of sample (c) before and after (d) 2, (e) 4, (f) 6, (g) 8, and (h) 10 days of treatment

Comparison of the two visual photographs, carried out by a dental practitioner blinded to the study, indicated no obvious sign of mineral loss (i.e., white spot lesion) within the treatment window even after 10 days of demineralization, suggesting the insensitivity of the conventional visual inspection method to detection of early demineralization. However, the presence of a lesion is observed in the normalized TPLI amplitude images, confirming the ability of the LWIR TPLI system to identify early caries not detectable via visual inspection.

Figures 5.2(d)–5.2(h), show the normalized amplitude images taken at 2, 4, 6, 8, and 10 days of treatment, respectively. The image sequence reveals an increasing trend in the contrast between the treated and intact tissue which is due to the enhanced light trapping, and consequently, higher light absorption within the demineralized enamel, leading to an enhanced signal amplitude in the treatment window. As the demineralization progresses, the treatment window becomes more discernible in the TPLI amplitude images as a result of expansion of the caries lesion into the enamel.

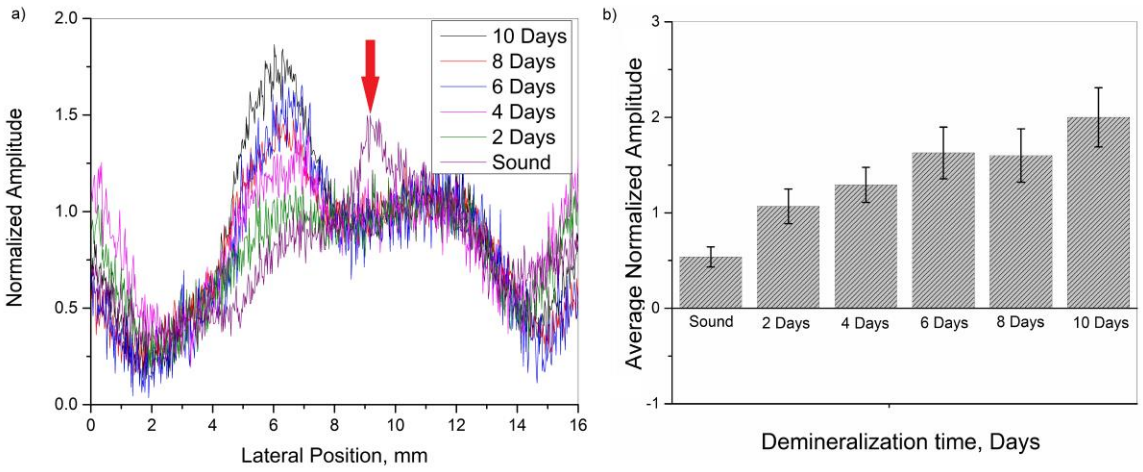

Figure 5.3 (a) Amplitude profiles along the dashed line shown in Figure 5.2(h) and (b) the average normalized amplitude values within the treatment window

Such increasing trend can also be seen in the transverse normalized amplitude profiles of Figure 5.3(a) plotted along the dashed line indicated in Figure 5.2(h) as well as the average normalized amplitude values calculated within the treatment window shown in Figure 5.3(b). Looking at the amplitude profiles for different demineralization stages, it can be realized that there are large variations in the amplitude values which make the treatment stages less distinguishable from each other. Such behavior in the amplitude profiles is due

to the spatial and day-to-day variations in surface properties (e.g., emissivity) of enamel, making the non-emissivity normalized amplitude channel less sensitive to changes in the extent of demineralization between different treatment times. Although, different treatment stages can be realized from the average normalized amplitude bar plots, they can hardly be statistically differentiated due to overlapping of the error bars. The other issue with the non-emissivity normalized nature of the amplitude channel is its sensitivity to surface stains. Presence of a stain with a different emissivity can be realized by comparing the amplitude profiles for sample before and after treatment where there is a spike in the profile outside of the treatment window (indicated by an arrow in figure 5.3(a)). This feature is disappeared in the next stages as a result of proper cleaning of the imaged surface.

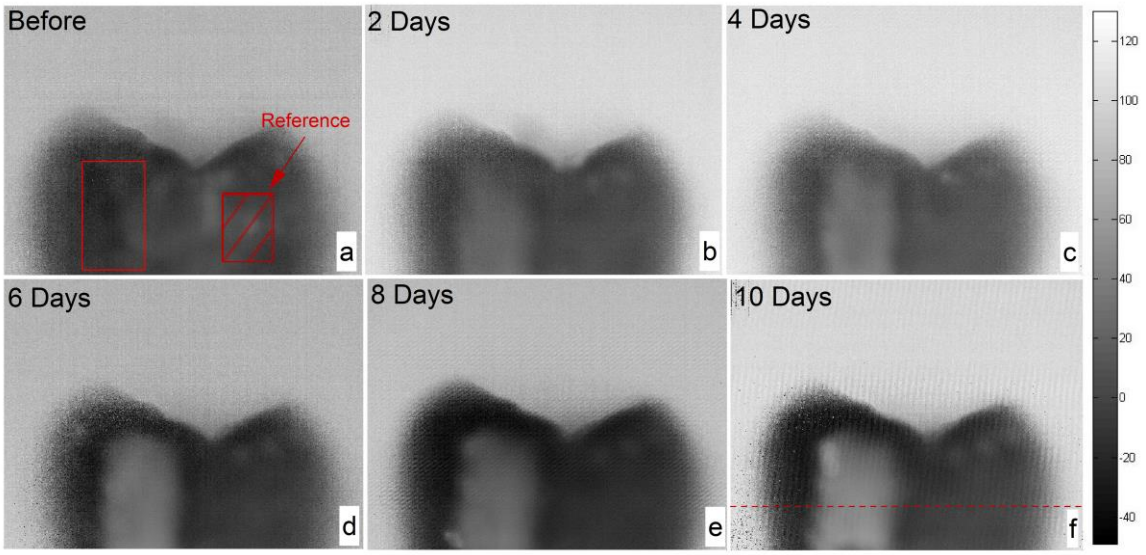

Figure 5.4 TPLI Phase images of sample with proximal caries(a) before and after (b) 2, (c) 4, (d) 6, (e) 8, and (f) 10 days of treatment

Figures 5.4(b)–5.2(f), show the TPLI phase images taken at 2, 4, 6, 8, and 10 days of treatment, respectively. It should be noted that the same contrast mapping has been applied to all images of Figure 5.2 and 5.4 to ensure the validity of comparison between the images. Careful inspection of the image sequence obtained at different stage of demineralization reveals that as the treatment time increases the caries lesion becomes more apparent while the intact areas in the images appear with a similar contrast. This monotonic increase in the average phase values is due to the substitution of hydroxyapatite crystals from close-to-surface enamel with micro-cavities leading to an increase in the demineralized lesion depth which enhances local light scattering and absorption near the surface. As the demineralized region's thickness increases, the thermal-wave centroid shifts farther away from the surface, resulting in an increase in the phase lag between the optical excitation (i.e., reference signal) and the acquired infrared response signal.

To further demonstrate the changes in phase values over various stages of demineralization progression, figure 5.5(a) plots the transverse phase profiles at different stages of artificial demineralization along the dashed line shown in figure 5.4(f). The profiles clearly verify the presence of a caries lesion within the treatment window. It can be seen that as demineralization progresses, the thermophotonic phase values increase within the treatment window while the phase values remain approximately the same at intact regions. Comparing the phase profiles of figure 5.5(a) with amplitude profiles of figure 5.3(a), one can realize that the phase profiles exhibit less variations compared to the amplitude profiles, making the different treatment stages more discernible from each other. Moreover, by looking at the average phase and amplitude plots the different treatment stages can

easily be recognized from the phase bar plots while these stages are less discernible from the average normalized amplitude plots. According to equation 3.1, the parameter “A” which is proportional to the emissivity of the interrogated surface in PTR/LIT, is cancelled out when calculating the phase values in the lock-in process. Emissivity normalized nature of the TPLI phase channel is makes it insensitive to variations in the thermophysical properties as well as the surface conditions of the sample which cause changes in the sample emissivity, and consequently, more sensitive to the changes in the demineralization between different treatment stages. However, the information of the amplitude images can be used to complement those of the phase images.

The increasing trend in the contrast between treated and intact areas can be quantitatively validated by comparing the average phase values within the treatment window for the untreated, 2, 4, 6, 8, and 10 days of treatment which are found to be -7.69, 16.54, 18.12, 38.75, 40.77, and 50.95 degrees (Figure 5.5(b)), respectively. The bar plots of figure 5.5(b) obtained from the mean phase values and their standard deviations over the treatment window are also confirming increase in phase values as more mineral is removed from enamel and thus manifesting the shift of the thermal-wave centroid away from the interrogated surface of enamel. The variations in the increasing trend in the bar plots is speculated to happen as a result of variations in the demineralizing effect of the acidic gel which is dependent on the ambient temperature as well as the sample properties.

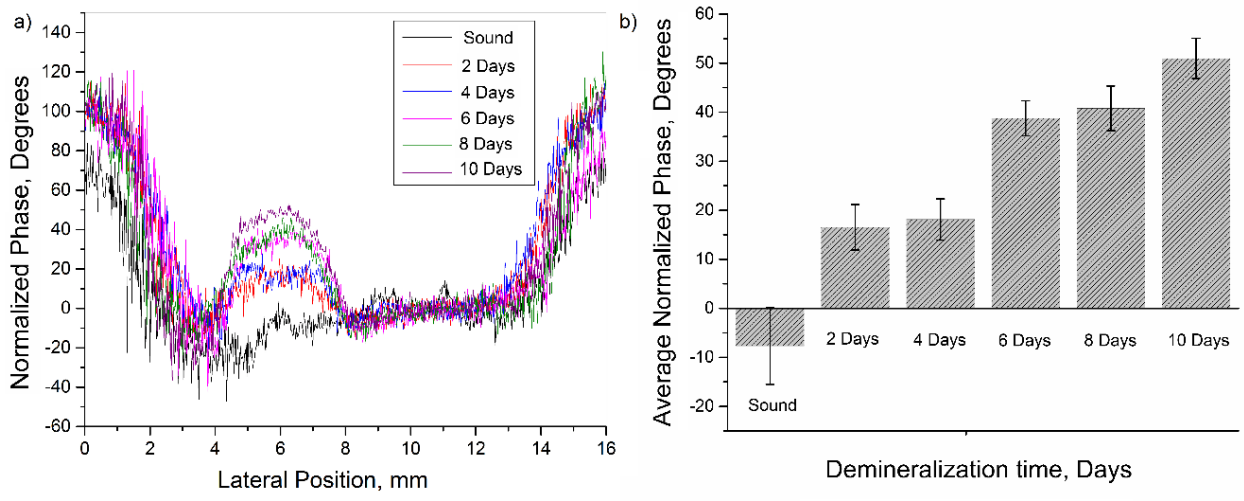

Figure 5.5 (a) Phase profiles along the dashed line shown in Figure 5.4(f) and (b) average phase values within the treatment window for samples at several demineralization stages

The obtained results demonstrate the ability of the developed low-cost LWIR TPLI system in detecting early proximal caries not detectable via visual inspection.

5.3.2 Detection of occlusal caries

Occlusal caries are the most prevalent type of dental caries which can progress deep into the enamel and form a cavity. The significance of detection of early occlusal caries lies in the fact that this surface cannot directly be inspected via X-ray radiography. Since X-ray radiography works based on the transmission of radiation though the enamel, proper interrogation of occlusal surface requires the detector to be placed beneath the occlusal surface which is not feasible in dental practice. However, TPLI operates in reflection mode and can thus directly interrogate the occlusal surface via proper optical design of the imaging device which can potentially include a combination of an inclined mirror for directing infrared emission into the camera and an optical fiber for laser light delivery.

In order to demonstrate the ability of the developed low-cost thermophotonic imaging system to detect early occlusal caries, a 10-day demineralization procedure, similar to that applied to proximal tooth surface, is applied on a treatment window placed on the occlusal surface of a relatively healthy sample (indicated in Figure 5.6(a)). Figure 5.6(b) shows a photograph of the sample after 10 days of treatment. No visual indication of demineralization is observed in this image. On the contrary, the inception and progression of early occlusal caries is clearly evident in the TPLI images. Figures 5.6(c)-5.6(h) exhibit a similar trend to that of proximal caries in terms of the increase in contrast between the treatment window and intact areas as the treatment time increases. However, due to the variations in physical and structural properties of the occlusal surface and its complex geometry the extent of demineralization is variable throughout the treatment window. Yet, the increase in overall phase shift can be realized from the average phase values within the treatment window shown in Figure 5.7. The relatively large standard deviation present in Figure 5.7 is due to the non-uniformity of demineralization throughout the treatment window and complex structure of the occlusal surface, leading to significant variations in the obtained phase values, and consequently, larger standard deviations.

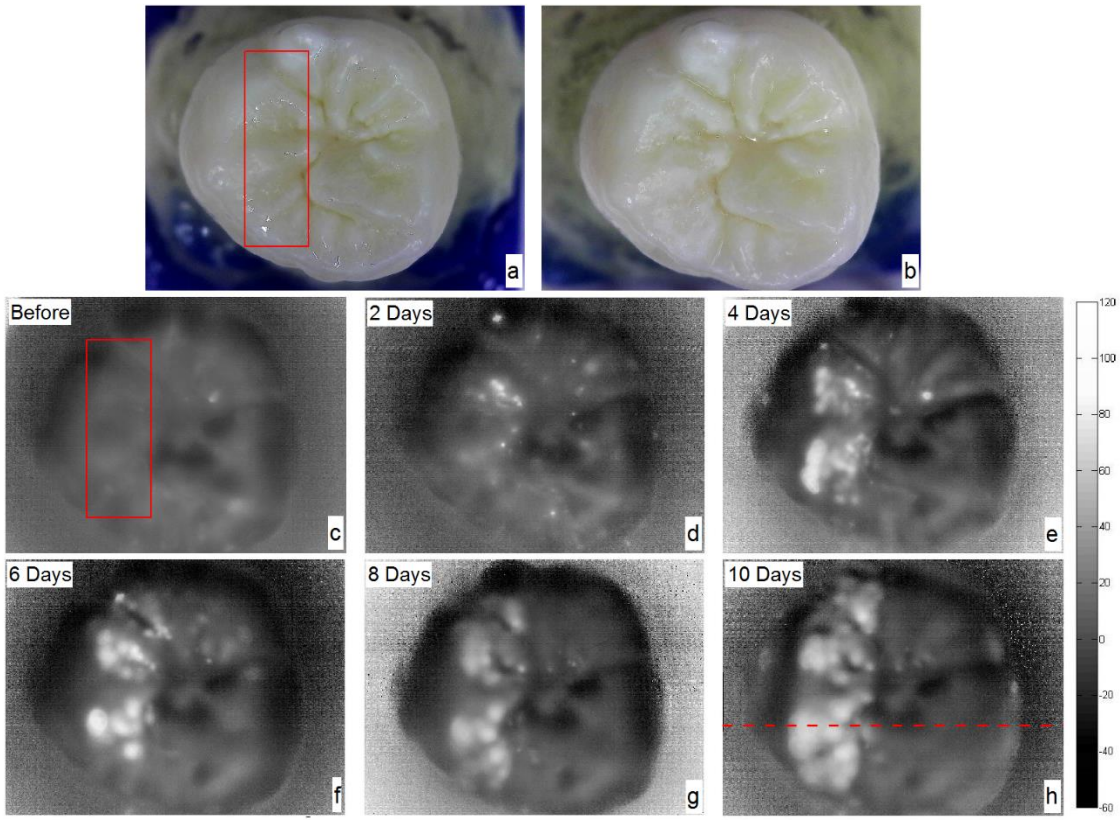

Figure 5.6 Optical image of the sample (a) before and (b) after 10 days of demineralization on the treatment window. TPLI phase images of sample (c) before and after (d) 2, (e) 4, (f) 6, (g) 8, and (h) 10 days of treatment obtained at 2 Hz modulation frequency

The obtained results from this study, as the first controlled demineralization imaging investigation on occlusal caries, suggest the potential of the developed LWIR TPLI system in probing early occlusal caries frequently encountered in the clinical practice.

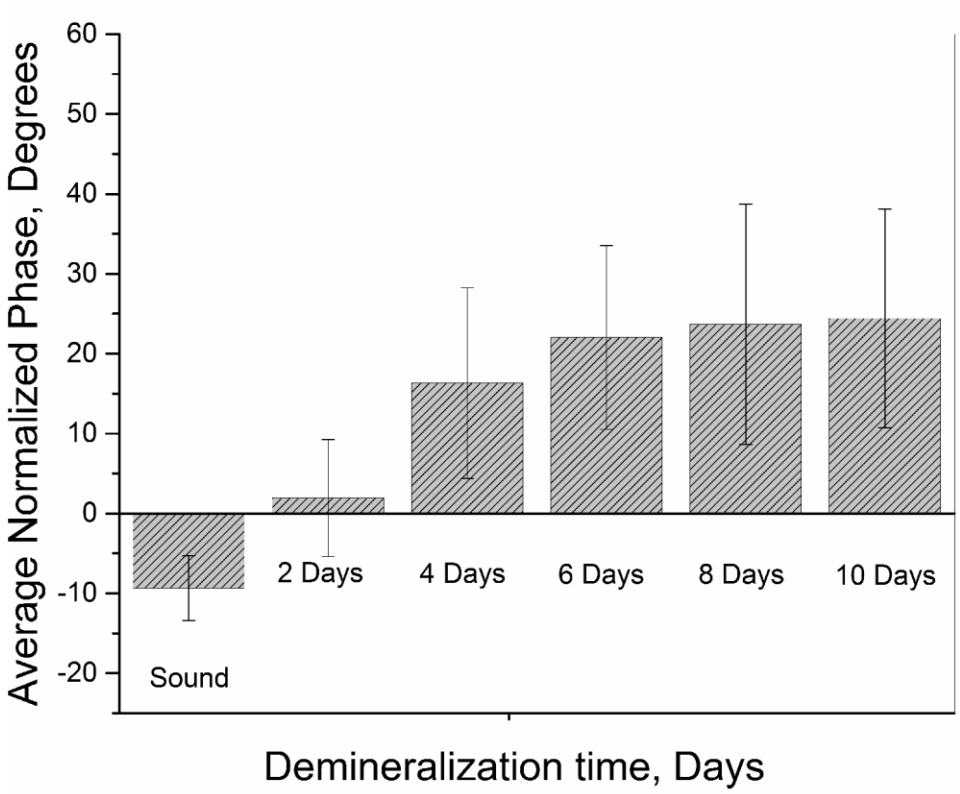

Figure 5.7 Average phase values within the treatment window for samples at several demineralization stages

5.3.3 Detection of Natural Occlusal Caries

Figure 5.8 presents the TPLI amplitude and phase images obtained from a tooth with suspected natural caries at 1 Hz, 5 Hz, and 20 Hz modulation frequencies. Unlike the previous sample, the occlusal surface of this sample is investigated at its natural state (no artificial demineralization is applied). As depicted in the photograph (Figure 5.8(a)), occlusal pit and fissures (e.g., features 1 and 2) can be identified on the occlusal surface of the sample; however, no visual evidence of mineral loss (e.g., white spot lesions) can be observed by visual inspection. Figures 5.8(b) and 5.8(e) depict the TPLI amplitude and

phase images obtained at 1 Hz, respectively. Features can hardly be resolved in these blurry amplitude and phase images due to the long thermal diffusion length at 1Hz. At low modulation frequencies, thermal-waves face less spatial attenuation and therefore effectively probe deeper into the enamel, yielding superposed contributions from subsurface features within the long thermal diffusion length. To avoid the interfering effects of deep features (supposedly from dentin [48, 53]), the thermal diffusion length is reduced by imaging at 5 Hz and 20 Hz to interrogate the clinically-relevant near-surface regions of the occlusal surface. Considerable improvement in the axial resolution is clearly evident in both amplitude and phase images obtained at higher frequencies (Figures 5.8(c), 5.8(d), 5.8(f), and 5.8(g)).

Features 1 and 2 are healthy-looking occlusal pit and fissures which appear to be demineralized based on the LWIR TPLI amplitude and phase images. The enhanced local optical absorption at these caries sites increases the thermal-waves amplitude and shifts the thermal-wave centroid causing the diagnostic contrast in the amplitude and phase images. Comparison of the phase images obtained at different frequencies suggests that features 1 and 2 are perhaps early caries located very close to surface as they appear more resolved in the 20Hz phase image with the shortest thermal diffusion length (Figure 5.8(g)).

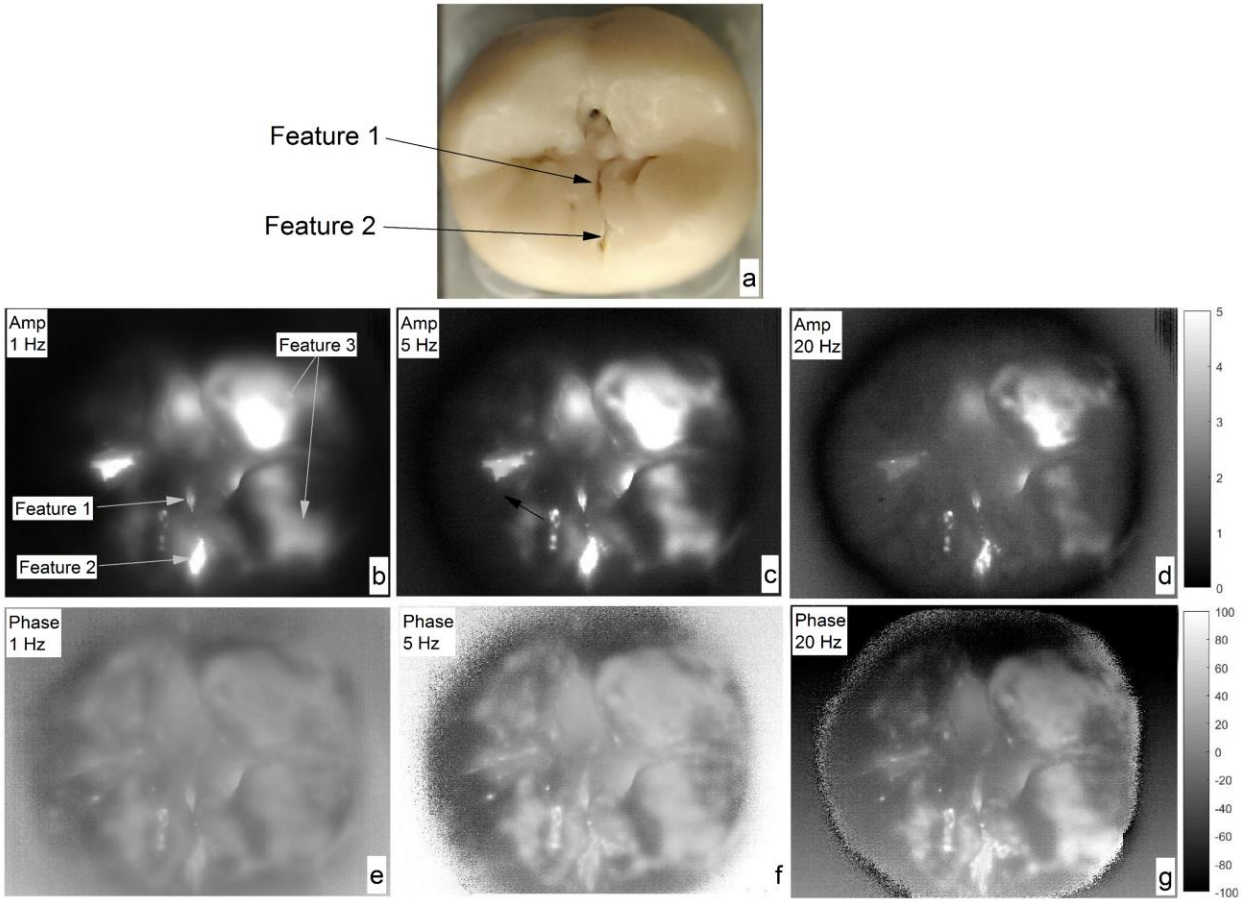

Figure 5.8 Optical image (a) of the occlusal surface of tooth sample. Thermophotonic amplitude (b) and phase (e) images of the occlusal surface obtained at 1 Hz. Thermophotonic amplitude (c) and phase (f) images of the occlusal surface obtained at 5 Hz. Thermophotonic amplitude (d) and phase (g) images of the occlusal surface obtained at 20 Hz.

Although the occlusal surface of the tooth (Figure 5.8(a)) looks relatively healthy, appearance of two bright spots in the phase and amplitude images (feature 3 in figures 5.8(d) and 5.8(g)) suggests the presence of a demineralized area at the occlusal cusps. These suspected early caries also appear to be very close to surface as their shape and

outline is revealed only at the highest modulation frequency (Figures 5.8(e) and 5.8(f) vs. figure 5.8(g)). The presented results are in agreement with those of Tabatabaei et al. [28] from teeth with natural caries which were verified by TMR.

Comparing the TPLI amplitude and phase images obtained from this sample, it can be understood that the phase images are able to resolve more features than amplitude images due to emissivity normalized nature of the TPLI phase channel which is in accordance with the results obtained from amplitude and phase profiles for sample with proximal caries, images of Figure 5.8.

The obtained results from occlusal surface imaging suggest the potential of the developed LWIR TPLI system in probing natural occlusal caries which is most commonly encountered in the clinical practice.

5.3.4 Determination of Detection Threshold

The presented results in previous sections for the controlled demineralization studies of proximal and occlusal caries indicate that the developed TPLI system using a low-cost LWIR camera is capable of detecting early caries. Another important parameter of a diagnostic modality is its detection threshold (i.e., how early the system can detect caries). To this end, a time-dependent controlled demineralization procedure is followed in small intervals (four- and six-hour) up to 2 days of treatment to create minute amounts of demineralization in a rectangular window located on the proximal surface of a dental sample. Similar to the previous results, it was observed that as the treatment time increases, the phase contrast between the treatment window and the intact regions increases due to

the progression of the artificially-induced early caries lesion into the enamel (Figure 5.9). Bar plots of Figure 5.9 along with their standard deviations indicate that before 12 hours of treatment the system is not sensitive enough to statistically differentiate between the healthy and demineralized tissues as the average phase values of the 4- and 8-hour treated windows fall within the standard deviation of phase values obtained from the untreated sample. However, after application of demineralization for 12 hours or more, the early caries can be statistically differentiated due to an increase in the average phase values above the detection threshold of the imaging system. The instability in the average phase value trend appears to be consistent with the concurrent occurrence of demineralization and remineralization cycles proposed by the early caries mechanism theories [33]. The obtained results suggest the suitability of the developed system in detection of very early demineralization and its high sensitivity compared to its counterparts such as OCT which is limited to detect caries lesions only after 24 hours of treatment with acidic gel [49].

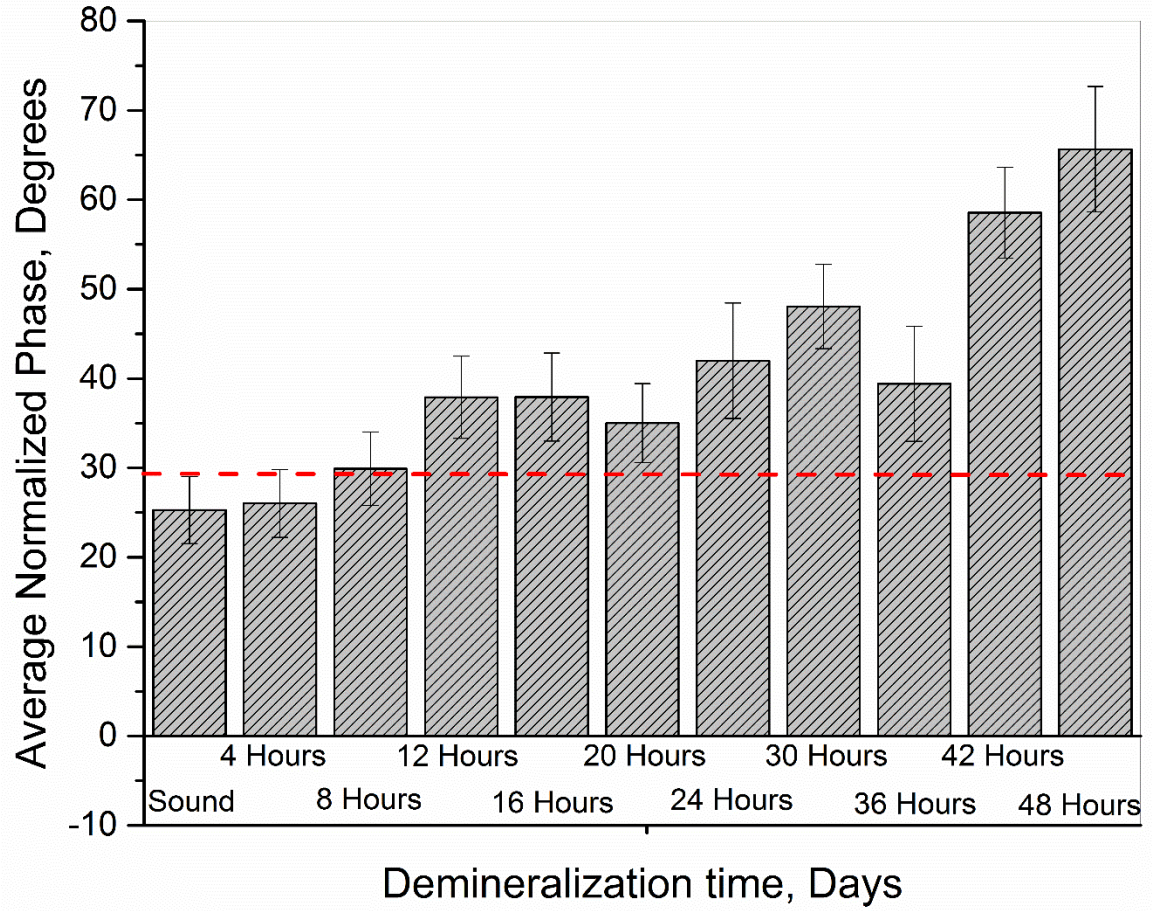

Figure 5.9 Average phase values within the treatment window for the sample at several demineralization stages. The dashed line indicates the detection threshold of our low-cost LWIR TPI system.

Chapter 6

Conclusion, Shortcomings, and Future Directions

This chapter provides the conclusions and the important results obtained in this research. Shortcomings of developed system along with the potential directions for future works in this area are also discussed.

6.1 Conclusion

In this thesis, a low-cost thermophotonic lock-in imaging system for detection of early dental caries using an inexpensive LWIR infrared camera is presented. This study, to the best of our knowledge, is the first report on the application of active thermography in the LWIR band for diagnostic imaging of biological samples (i.e., detection of early dental caries). The overall cost of the developed LWIR TPLI system (~USD $15k) is significantly reduced in comparison to the highly expensive (~USD $100k) existing MWIR technology. Through theoretical modelling, we have demonstrated that thermophotonic detection of early dental caries in the LWIR band leads to improvement in the detection sensitivity compared to the previously reported systems detecting in the MWIR band. Then, capabilities of this non-contact, non-invasive diagnostic system are demonstrated through experiments carried out on biological and non-biological samples. The diagnostic performance of the developed LWIR TPLI system was first verified using standard samples. In the step, the system was used to monitor the formation and progression of artificially-induced early proximal as well as natural and artificially-induced occlusal dental caries. The follow-up in vitro experiments confirm the sensitivity of our non-contact

and non-invasive diagnostic imaging system to early demineralization, not detectable via conventional clinical inspection methods. The obtained results also suggest that LWIR TPLI is able to effectively probe the occlusal surface of tooth which cannot be directly imaged via X-ray radiography. The detection threshold study also suggests that the developed system is capable of detecting artificially-induced caries of greater than 12 hours. In conclusion, the developed low-cost imaging system is able to provide reasonable contrast and sensitivity to early caries lesions mostly encountered in dental practice and has great potential for integration into a commercially and clinically viable dental diagnostic imaging device.

6.2 Shortcomings and Future Directions

Despite of promising results obtained from probing early demineralization in dental hard tissues using the LWIR TPLI system, there are few shortcomings which have to be addressed in future. One of the major shortcomings of the developed LWIR TPLI system is its non-optimal measurement time. In order to produce images with optimal SNR, the number of image sequences to be averaged along with the average intensity of the laser have to be optimized. Increasing the average laser intensity will lead to enhanced heat generation and formation of thermal-waves with higher amplitude in the sample which can produce stronger signals as detected by the infrared camera. However, according to dental literature [6], the maximum allowable average optical intensity for clinically relevant conditions is limited to intensities by which an intrapulpal temperature increase of less than 5°C is induced in the tooth. As such, the best compromise between the average laser intensity and the number of averaging/measurement time should be found experimentally.

The other issue with the sacrifice one has to make between the resolution and the ability to inspect deep into a sample. That is, low frequency thermal-waves can penetrate deep into the tissue but their response suffers from poor diffusive resolution, while at high frequencies the resolution is improved at the cost of shallow inspection depth. As such, for proper identification of the relative depth of different caries, a complete frequency scan through several experiments is to be carried out. This process is very time consuming and therefore limits the clinical incorporation of the TPLI system. To properly address this issue and with the aim of improving the dynamics range of the imaging system, the thermal-wave radar techniques need to be added to the system in the next step. The linear frequency modulation and Binary Phase Coded excitation along with Radar matched filtering techniques will enable achieving better imaging resolution while inspecting deep in samples.

The future directions for this project to be done over coming years would be the incorporation of Radar techniques to be used for monitoring the controlled demineralization on proximal, occlusal, and interproximal tooth surfaces and to generate three dimensional thermograms of caries for a number of dental samples. Finally, the developed imaging system will be ready to be translated into a clinically and commercially viable dental diagnostic device with reasonable accuracy and reliability. This device is expected to be a convenient and easy-to-operate caries inspection tool to be used by clinicians and can be integrated into a dental console to produce TPLI images of different types of teeth in the oral cavity. A conceptual design for such clinical system is illustrated in Figure 6.1.

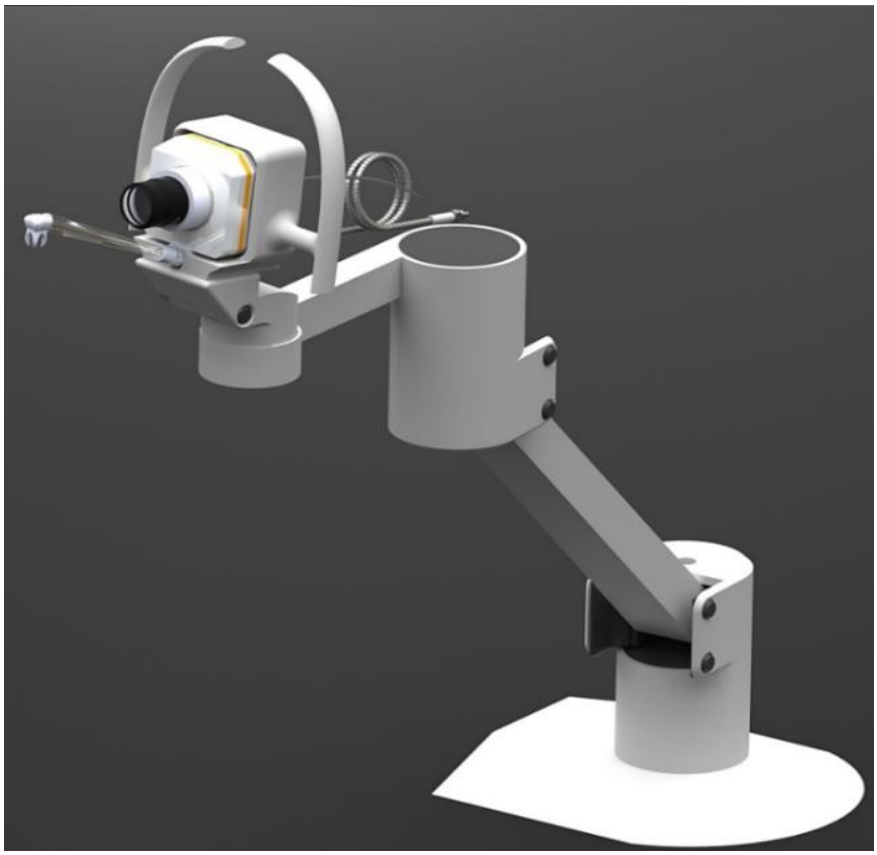

Figure 6.1 Designed clinically viable imaging platform

References

1. Schmitz, B. and G. Goch, *PHOTOTHERMAL RADIOMETRY–PRINCIPLE AND APPLICATIONS.*

2. Bell, A.G., *On the production and reproduction of sound by light.* American Journal of Science, 1880(118): p. 305-324.

3. Rosencwaig, A. and A. Gersho, *Theory of the photoacoustic effect with solids.* The Journal of the Acoustical Society of America, 1975. **58**(S1): p. S52-S52.

4. Maris, H. and S. Balibar, *Diffusion waves and their uses.* Physics today, 2000. **53**(8): p. 29-34.

5. Imhof, R., B. Zhang, and D. Birch, *Photothermal radiometry for NDE.* Non-Destructive Evaluation, 1994. **2**: p. 185-236.

6. Tabatabaei, N., *Development of Frequency and Phase Modulated Thermal-wave Methodologies for Materials Non-destructive Evaluation and Thermophotonic Imaging of Turbid Media*. 2012, University of Toronto.

7. Fourier, J., *Theorie analytique de la chaleur, par M. Fourier*. 1822: Chez Firmin Didot, père et fils.

8. Angström, A., *XVII. New method of determining the thermal conductibility of bodies.* The London, Edinburgh, and Dublin Philosophical Magazine and Journal of Science, 1863. **25**(166): p. 130-142.

9. Busse, G., *Optoacoustic phase angle measurement for probing a metal.* Applied Physics Letters, 1979. **35**(10): p. 759-760.

10. Rosencwaig, A. and G. Busse, *High-resolution photoacoustic thermal-wave microscopy.* Applied Physics Letters, 1980. **36**(9): p. 725-727.

11. Busse, G. and P. Eyerer, *Thermal wave remote and nondestructive inspection of polymers.* Applied Physics Letters, 1983. **43**(4): p. 355-357.

12. Busse, G. *From photothermal radiometry to lock-in thermography methods*. in *Journal of Physics: Conference Series*. 2010. IOP Publishing.

13. Carlomagno, G. and P.G. Berardi. *Unsteady thermotopography in non-destructive testing*. in *Proc. 3rd Biannual Exchange, St. Louis/USA*. 1976.

14. Beaudoin, J.L., et al. *Numerical system for infrared scanners and application to the subsurface control of materials by photothermal radiometry*. in *1985 International Technical Symposium/Europe*. 1986. International Society for Optics and Photonics.

15. Kuo, P., et al., *Parallel thermal wave imaging using a vector lock-in video technique,* in *Photoacoustic and Photothermal Phenomena*. 1988, Springer. p. 415-418.

16. Busse, G., D. Wu, and W. Karpen, *Thermal wave imaging with phase sensitive modulated thermography.* Journal of Applied Physics, 1992. **71**(8): p. 3962-3965.

17. Karpen, W., et al. *Depth profiling of orientation in laminates with local lockin thermography*. in *Proc. QIRT*. 1994.

18. Wu, D., *Lockin thermography for defect characterization in veneered wood.* Proceedings of Quantitative infrared thermography, 1994. **94**: p. 298ą302.

19. Wu, D., et al., *Applications of lockin-thermography methods*, in *Review of progress in quantitative nondestructive evaluation*. 1996, Springer. p. 511-518.

20. Meola, C. and G. Carlomagno, *The Role of Infrared Thermography in NDT*, in *Nondestructive Testing of Materials and Structures*. 2013, Springer. p. 91-96.

21. Wu, D., et al., *Inspection of aircraft structural components using lockin-thermography.* Quantitative infrared thermography, QIRT, 1996. **96**: p. 251-256.

22. Bison, P., S. Marinetti, and E. Grinzato, *Measurement of thermal diffusivity by lock-in thermography.* Proc. QIRT 2000, 2000: p. 30-5.

23. Meola, C., et al., *Nondestructive evaluation of fiber reinforced polymers with lockin thermography*, in *Residual Stress, Thermomechanics & Infrared Imaging, Hybrid Techniques and Inverse Problems, Volume 8*. 2014, Springer. p. 207-213.

24. Giorleo a, G., C. Meola b*, and A. Squillace a, *The use of lock-in thermography in industrial applications.* Nondestructive Testing and Evaluation, 2000. **16**(1): p. 15-29.

25. An, Y.-K., J.M. Kim, and H. Sohn, *Laser lock-in thermography for detection of surface-breaking fatigue cracks on uncoated steel structures.* Ndt & E International, 2014. **65**: p. 54-63.

26. John, C. and A. Salerno. *Raw data set of thermal wave propagation in hard dental tissues*. in *Proc. of 11th Int. Symp. and Exhibition for Computer Assisted Radiology (CAR97)*. 1997.

27. John, C., et al., *Applying phase sensitive modulated thermography to ground sections of a human tooth*, in *Nondestructive Characterization of Materials VIII*. 1998, Springer. p. 757-762.

28. Tabatabaei, N., A. Mandelis, and B.T. Amaechi, *Thermophotonic lock-in imaging of early demineralized and carious lesions in human teeth.* Journal of biomedical optics, 2011. **16**(7): p. 071402-071402-10.

29. Tabatabaei, N., A. Mandelis, and B.T. Amaechi, *Thermophotonic radar imaging: An emissivity-normalized modality with advantages over phase lock-in thermography.* Applied Physics Letters, 2011. **98**(16): p. 163706.

30. Tabatabaei, N., et al., *On the sensitivity of thermophotonic lock-in imaging and polarized Raman spectroscopy to early dental caries diagnosis.* Journal of biomedical optics, 2012. **17**(2): p. 0250021-0250025.

31. Fried, D., et al. *Near-IR imaging of interproximal lesions from occlusal surfaces and the influence of stains and plaque*. in *Biomedical Optics 2006*. 2006. International Society for Optics and Photonics.

32. Fried, D., et al., *Imaging caries lesions and lesion progression with polarization sensitive optical coherence tomography.* Journal of biomedical optics, 2002. **7**(4): p. 618-627.

33. Fejerskov, O. and E. Kidd, *Dental caries: the disease and its clinical management*. 2009: John Wiley & Sons.

34. Featherstone, J.D., *Prevention and reversal of dental caries: role of low level fluoride.* Community dentistry and oral epidemiology, 1999. **27**(1): p. 31-40.

35. Abanto, J., et al., *Impact of oral diseases and disorders on oral health-related quality of life of preschool children.* Community dentistry and oral epidemiology, 2011. **39**(2): p. 105-114.

36. Prevention, O.o.D. and H. Promotion, *US Department of Health and, Human Services: Healthy people 2020.* Office of Disease Prevention and Health Promotion, US Department of Health and Human Services, 2011.

37. Health, N.I.o., *Dental Caries (Tooth Decay) in Adults (Age 20 to 64).* 2008.

38. White, S.C. and M.J. Pharoah, *Oral radiology: principles and interpretation*. 2014: Elsevier Health Sciences.

39. Panel, N.I.o.H.C.D., *National Institutes of Health Consensus Development Conference statement: diagnosis and management of dental caries throughout life, March 26–28, 2001*. The Journal of the American Dental Association, 2001. **132**(8): p. 1153-1161.

40. Joyston-Bechal, A., E. Kidd, and S. Joyston-Bechal, *Essentials of dental caries: the disease and its management*. 1998, Oxford: Oxford University Press.

41. Kidd, E. and O. Fejerskov, *What constitutes dental caries? Histopathology of carious enamel and dentin related to the action of cariogenic biofilms.* Journal of dental research, 2004. **83**(suppl 1): p. C35-C38.

42. Minet, O., K. Dörschel, and G. Müller, *Lasers in biology and medicine.* Laser Applications. Landolt–Börnstein, 2004. **8**: p. 279-310.

43. Jones, R.S. and D. Fried. *Attenuation of 1310-and 1550-nm laser light through sound dental enamel*. in *International Symposium on Biomedical Optics*. 2002. International Society for Optics and Photonics.

44. Featherstone, J.D. and D. Fried, *Fundamental Interactions of Laserswith Dental Hard Tissues.* Medical laser application, 2001. **16**(3): p. 181-194.

45. Hellen, A., *Quantitative Evaluation of Simulated Enamel Demineralization and Remineralization Using Photothermal Radiometry and Modulated Luminescence*. 2010, University of Toronto.

46. Amaechi, B., S. Higham, and W. Edgar, *Efficacy of sterilisation methods and their effect on enamel demineralisation.* Caries research, 1998. **32**(6): p. 441-446.

47. Bader, J.D., D.A. Shugars, and A.J. Bonito, *A systematic review of the performance of methods for identifying carious lesions.* Journal of public health dentistry, 2002. **62**(4): p. 201-213.

48. Hall, A. and J. Girkin, *A review of potential new diagnostic modalities for caries lesions.* Journal of Dental Research, 2004. **83**(suppl 1): p. C89-C94.

49. Amaechi, B.T., *Emerging technologies for diagnosis of dental caries: The road so far.* Journal of Applied Physics, 2009. **105**(10): p. 102047.

50. Kaiplavil, S. and A. Mandelis, *Truncated-correlation photothermal coherence tomography for deep subsurface analysis.* Nature Photonics, 2014. **8**(8): p. 635-642.

51. Meller, C., et al., *A new in vivo method for measuring caries activity using quantitative light-induced fluorescence.* Caries research, 2006. **40**(2): p. 90-96.

52. Matvienko, A., et al., *Theoretical analysis of coupled diffuse-photon-density and thermal-wave field depth profiles photothermally generated in layered turbid dental structures.* Journal of Applied Physics, 2009. **105**(10): p. 102022.

53. Breitenstein, O. and M. Langenkamp, *Lock-in thermography: basics and use for functional diagnostics of electronic components*. Vol. 10. 2003: Springer Science & Business Media.

54. Amaechi, B., S. Higham, and W. Edgar, *Factors affecting the development of carious lesions in bovine teeth in vitro.* Archives of oral biology, 1998. **43**(8): p. 619-628.

55. Hellen, A., A. Mandelis, and Y. Finer. *Photothermal radiometry and modulated luminescence examination of demineralized and remineralized dental lesions*. in *Journal of Physics: Conference Series*. 2010. IOP Publishing.

56. Jeon, R.J., et al. *Experimental investigation of demineralization and remineralization of human teeth using infrared photothermal radiometry and modulated luminescence*. in *Biomedical Optics (BiOS) 2008*. 2008. International Society for Optics and Photonics.

57. Amaechi, B.T., et al., *Application of optical coherence tomography for imaging and assessment of early dental caries lesions.* Laser physics, 2003. **13**(5): p. 703-710.

58. Mandelis, A., *Diffusion-wave fields: mathematical methods and Green functions*. 2013: Springer Science & Business Media.

59. Tabatabaei, N. and A. Mandelis, *Thermal coherence tomography using match filter binary phase coded diffusion waves.* Physical review letters, 2011. **107**(16): p. 165901.

60. Prahl, S., et al., *Determination of optical properties of turbid media using pulsed photothermal radiometry.* Physics in medicine and biology, 1992. **37**(6): p. 1203.